SANDIA REPORT
SAND2016-1753
Unlimited Release
Printed February 2016

Carbon Composite Microelectromechanical Systems (CMEMS)

Christopher Dyck, Cody Washburn, Patrick Finnegan, Kent Pfeifer, Jill Blecke, Michael Rector, Michael Satches, Lee Massey, and Thomas Beechem

Prepared by
Sandia National Laboratories
Albuquerque, New Mexico 87185 and Livermore, California 94550

Sandia National Laboratories is a multi-program laboratory managed and operated by Sandia Corporation, a wholly owned subsidiary of Lockheed Martin Corporation, for the U.S. Department of Energy's National Nuclear Security Administration under contract DE-AC04-94AL85000.

Issued by Sandia National Laboratories, operated for the United States Department of Energy by Sandia Corporation.

Available to DOE and DOE contractors from
U.S. Department of Energy
Office of Scientific and Technical Information
P.O. Box 62
Oak Ridge, TN 37831

Telephone: (865) 576-8401
Facsimile: (865) 576-5728
E-Mail: reports@osti.gov
Online ordering: http://www.osti.gov/scitech

Available to the public from
U.S. Department of Commerce
National Technical Information Service
5301 Shawnee Rd
Alexandria, VA 22312

Telephone: (800) 553-6847
Facsimile: (703) 605-6900
E-Mail: orders@ntis.gov
Online order: http://www.ntis.gov/search

SAND2016-1753
Unlimited Release
Printed February 2016

Carbon Composite Microelectromechanical Systems (CMEMS)

Christopher Dyck, Cody Washburn, and Michael Rector
Applied Technologies, Org. 5965

Patrick Finnegan
Organic Materials Science, Org. 1853

Kent Pfeifer
Bio/Chem/Physical Microsensors, Org. 1714

Thomas Beechem
Nanoscale Sciences Department, Org. 1124

Jill Blecke and Michael Satches
Component Science and Mechanics, Org. 1526

Lee Massey
Materials Chemistry, Org. 8223

Sandia National Laboratories
P.O. Box 5800
Albuquerque, New Mexico 87185-MS1212

Abstract

Pyrolyzed carbon as a mechanical material is promising for applications in harsh environments. In this work, we characterized the material and developed novel processes for fabricating carbon composite micro-electromechanical systems (CMEMS) structures. A novel method of increasing Young's modulus and the conductivity of pyrolyzed AZ 4330 was demonstrated by loading the films with graphene oxide prior to pyrolysis. By incorporating 2 wt.% graphene stiffeners into the film, a 65% increase in Young's modulus and 11% increase in conductivity were achieved. By reactive ion etching pyrolyzed blanket AZ 50XT thick film photoresist, a high aspect ratio process was demonstrated with films >7.5um thick. Two novel multi-level, volume-scalable CMEMS processes were developed on 6" diameter wafers. Young's modulus of 23 GPa was extracted from nanoindentation measurements of pyrolyzed AZ 50XT films. The temperature-dependent resistance was characterized from room temperature to 500C and found to be nearly linear over this range. By fitting the results of self-heated bridges in an inert

ambient, we calculated that the bridges survived to 1000C without failure. Transmission electron microscopy (TEM) results showed the film to be largely amorphous, containing some sub-micrometer sized graphite crystallites. This was consistent with our Raman analysis, which also showed the film to be largely sp^2 bonded. The calculated average density of pyrolyzed AZ 4330 films was 1.32 g/cm^2. Thin level of disorder and the conductivity of thin film resistors were found to unchanged by 2Mrad gamma irradiation from a Co_{60} source. Thin film pyrolyzed carbon resistors were hermetically sealed in a nitrogen ambient in 24-pin dual in-line packages (DIP's). The resistance was measured periodically and remained constant over 6 months' time.

ACKNOWLEDGMENTS

The authors would like to acknowledge Paul Resnik (MEMS Technologies), Scott Habermehl and Tom Friedmann (both in MESAFAB Operations 3), and Chuck Walker (Metallurgy & Materials Joining) for their help in developing and realizing the 6" diameter wafer processes, Tom Buchheit (Materials Mechanics & Tribology) for nanoindentation analysis, Greg Salazar (Microsystems Assessments I) for performing FIB and SEM work, and Mark Jenkins (Validation & Failure Analysis) for his help with the TCR measurements.

Supported by the Laboratory Directed Research and Development program at Sandia National Laboratories, a multi-program laboratory managed and operated by Sandia Corporation, a wholly owned subsidiary of Lockheed Martin Corporation, for the U.S. Department of Energy's National Nuclear Security Administration under contract DE-AC04-94AL85000.

CONTENTS

FIGURES

TABLES

1. INTRODUCTION

The pyrolysis of photo-patternable materials and the basic micro-electromechanical properties related to pyrolytic carbon materials and resonator device has been demonstrated by George Whitesides *et al.*[1]. Since then, Marc J. Madou *et al.*[2] and Richard L. McCreery *et al.*[3] have developed carbon on carbon approaches toward carbon microelectromechanical systems (MEMS), and high surface area electrochemical sensors, along with carbon for anode/cathode materials for Li-ion battery applications. Groups at Sandia have also demonstrated pyrolyzed carbon's potential bio-applications by electrochemically placing nano-materials on its' surface. [4].

The material is advantageous for MEMS in harsh environments because carbon is relatively chemically inert and capable of surviving high temperatures in non-oxidizing environments. The precursors are easily obtainable in the form of commercially available photoresists, and fabrication leverages many existing integrated circuit and MEMS fabrication processes. Relative to Si MEMS, the CMEMS field is relatively immature. Novel fabrication techniques need to be developed in order to realize practical MEMS sensors and actuators, and the material properties should be further characterized. To that end, the goal of this LDRD was to gain a better understanding of the material we were working with by measuring basic properties such as residual strain, density, Young's modulus, and the thermal coefficient of resistance (TCR), to characterize the material structure, and to develop novel and volume scalable processing capabilities.

Process development is discussed in Section 2. This includes methods for fabricating graphene-loaded films, thick films, and the development of volume scalable processes. Some basic properties of pyrolyzed photoresists are presented in Section 3. A study of graphene loaded pyrolyzed photoresists is presented in Section 4. The results of total dose gamma irradiated thin film resistors is discussed in Section 5, and the study of hermetically sealed thin film resistors is presented in Section 6.

2. PYROLYZED PHOTORESIST PROCESSING

We developed a number of processing techniques with a variety of photoresists over the course of the project. During the first year, we demonstrated that the pyrolyzed photoresist (PPR) properties of modulus and conductivity could be significantly varied by adding different amounts of graphene oxide prior to the pyrolysis process. The processing of these interesting films, known as graphene-loaded films, is discussed in Section 2.2. During the 2nd and 3rd years, we focused on developing thick film, high-aspect ratio processes, motivated by inertial sensor applications. During this time, break-through techniques such as reactive ion etching of PPR, thick film demonstrations, and volume processing on 6" wafers were demonstrated. This is discussed in Sections 2.3 and 2.4.

When designing inertial sensors, it is desirable to fabricate the structures out of thick films that can be patterned into features with high aspect ratios and vertical sidewalls, and that have low residual stress and stress gradient. Thick films lower the noise floor by increasing mass of the proof mass. High aspect ratio features with rectangular cross-sections are needed to separate in-plane and out-of-plane modes and minimize off-axis coupling. When electrostatic sensing is used, thick vertical sidewalls increase the drive and sense capacitance by increasing area and enabling narrow gaps to be patterned. Residual film stresses cause the structures to either contract (from tensile stress) or expand (from compressive stress) after the release process, leading to a deviation from the nominal design values of proof mass springs or mechanical interference between mechanical layers or between a mechanical layer and the substrate.

We started our development with films that were spin-deposited, soft-baked, and then photo patterned to define features and separations prior to the pyrolysis process. This is the easiest method used to pattern structures and works well for structures that move in and out of plane. However, this approach results in the poor lateral feature definition and cross-section because the photoresist reflows as the temperature is increased during the pyrolysis process. To solve this problem, a process was developed wherein blanket spin-deposited photoresist films were pyrolyzed before they were patterned. Then, reactive ion etching was used to pattern features after the pyrolysis process, which allowed us to fabricate thicker structures. Thicker films were achieved by applying photoresists using multiple spins and by using more viscous resists, such as 50XT.

During the aforementioned development, we were hampered by inconsistencies in the pyrolyzed films. Nominally similar/identical pre-pyrolysis processes, in terms of the type and thickness of the photoresist that was used, produced films that varied in quality from smooth films, well adhered to the substrate to blistered, cracked, or peeled carbon films. A significant amount of effort was expended to make re-producible films (in particular thick films). Experiments were conducted by varying the substrate and photoresist type, photoresist thickness, single vs. multiple photoresist spin depositions, etc…, which resulted in no clear trend relating the pre-pyrolysis conditions to the condition of the pyrolyzed films. Although we were successful in demonstrating films >7μm thick, these could be appropriately categorized as hero experiments.

The inconsistencies were ultimately attributed to uncontrolled (albeit unknown) conditions in the pyrolysis furnace we were using. When we switched to a furnace in 878, we achieved immediate and dramatic success, which directly led to our successful demonstration of volume scalable processes on 6" diameter silicon wafers.

2.1 PPR Films Fabricated out of AZ 4330

AZ4330, a positive photoresist manufactured by Microchemicals, was the most commonly pyrolyzed film over the course of the project to fabricate a variety of pyrolyzed carbon test structures (both loaded and unloaded). The photoresist were spin deposited, exposed, and developed in the Sandia MESA Microfab facility. This was done on quartz, bare silicon, silicon with an insulating layer of SiO_x deposited by plasma enhanced chemical vapor deposition (PECVD), and on silicon-on-insulator (SOI) substrates. The pyrolysis step was performed in a furnace in Bldg. 701 that accommodated 2" diameter wafers. A reducing ambient of 95%/5% N_2/H_2 was continually flowed during the process. The temperature was ramped linearly to 1000°C over 8 hours. It was then held for 1 hour at 1000°C before the furnace was turned off and the samples were allowed to passively cool. Resistors and were fabricated directly on either quartz or Si with an insulating layer of SiO_x. MEMS devices were fabricated on SOI wafers and released in xenon difluoride (XeF_4) gas. XeF_4 rapidly etches Si with high selectivity to organic and insulating films such as SiO_x and SiN. Anchors were formed by making large-area features, such as at the base of an array of cantilevers. The number of cycles during the XeF_4 release etch was monitored until the narrower features were released. In essence, this is a single level bulk micromachining process.

The changes in the patterned features during pyrolysis were characterized by measuring the decrease in the film thickness, the lateral shrinkage, and the change in the cross-section. The amount of material lost during the pyrolysis process was measured for 3 samples with spin-deposited AZ4330 photoresist at 6000, 7000, and 9000 rpm. The film thickness was measured before and after the pyrolysis process. The results summarized in Table 1 show an average thickness loss of 75.9%.

Table 1: Photoresist thickness decrease due to the pyrolysis

Spin rate [rpm]	Pre-pyrolysis thickness [µm]	Post-pyrolysis thickness [µm]	Thickness decrease [%]
6000	2.70	0.615	77.2
7000	2.52	0.610	75.8
9000	2.27	0.544	76.1

The change in the lateral dimensions of patterned features as a result of the pyrolysis process was characterized by resistor test structures under an optical microscope at 3 stages in the process: after developing the resist, after curing the photoresist, and after pyrolysis. The results are summarized in Figure 1. The width of resistor in Figure 1 (nominally 50µm wide by 200µm long) decreases by 0.6µm during the curing process and by another 0.8µm during pyrolysis. This is a small change (arguably within the measurement error of this size of a structure under an optical microscope), and is remarkable considering the nearly 76% decrease in the film thickness during pyrolysis.

It is apparent from the images in Figure 1 that the shape of the resistors changed during the curing process. The slight darkening at the edges of the structures makes them look more rounded. This was verified by examining the cross section of a broken cantilever (Figure 2), which revealed an airplane wing cross-section. This geometry also resulted when the curing

process was skipped. The change in shape was caused by the resist reflowing during the curing process (or during the pyrolysis process) as the temperature was increased above the photoresist's reflow temperature.

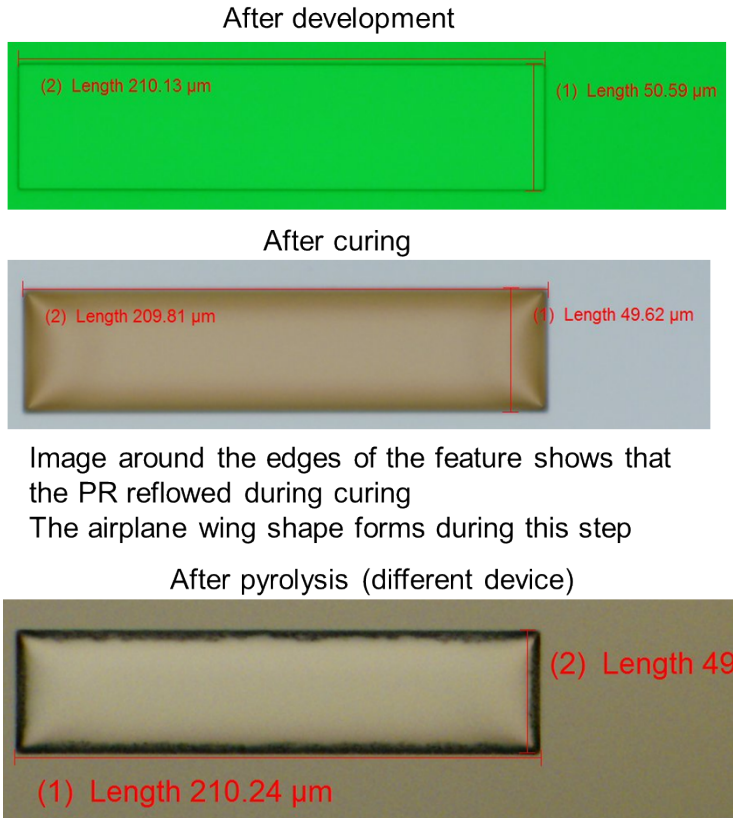

Area measurements before and after curing, and after pyrolysis

Resistors	Width	Length	X-Section Shape
Nominal	50	210	NA - layout
Before Cure	50.6	210	Rectangular
After Cure	50	210	Airplane wing
After Pyrolysis	49.1	210	Airplane wing

Figure 1: Optical micrograph images showing the lateral dimensional change of a resistor with nominal geometry of 50µm x 200µm.

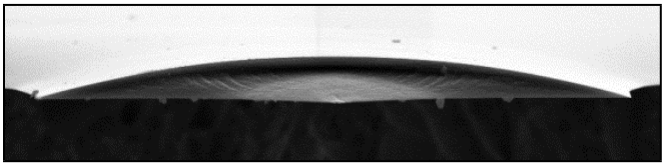

Figure 2: SEM image of a cantilever cross-section showing the airplane wing profile that results from photoresist reflow. This images was taken after the pyrolysis and release processes.

2.2 Graphene-Loaded PPR Processing

The modulus and conductivity of PPR films was increased by adding graphine oxide to photoresist prior to the spin deposition step. The following procedure was used to formulate the loaded photoresist [5]:

Improved reduced graphene oxide (iRGO) nanomaterial is dispersed into a photo-active polymer matrix using commercial novalac polymer sets for carbon composite MEMS patterning and device development. High temperature pyrolysis converts the iRGO sheet and photo-active

polymer into an amorphous carbon composite with disordered graphene sheets coupled into the matrix. Finally, an all carbon pattern is then released from the supporting substrate for testing. iRGO was synthesized following a recent literature report

Reduced graphene oxide (iRGO) was synthesized via the chemical reduction of improved graphene oxide (iGO) [6]. Approximately 600 mg of iGO was dispersed in deionized water (600 mL) and divided into two equal portions. These mixtures were stirred for approximately 24 hours followed by bath sonication for 1 hour. Immediately following sonication, the two portions were combined into a poly(methylpentene) Nalgene bottle (1 L capacity) and $N_2H_4 \cdot H_2O$ (3 mL) was added with stirring. The bottle was sealed, and the reaction was heated to 85°C in an oil bath for 24 hours with continuous stirring. Upon completion, the reaction was removed from the heat, cooled, and black solids were isolated by filtration through a coarse glass fritted funnel. The solid product was washed with deionized water (1 L), and methanol (500 mL) and dried at 60°C under vacuum. Additional aggregate solids that subsequently precipitated from the black filtrate were collected and washed as previously described. In general, the reaction yielded approximately 300 mg of iRGO.

2.3 Thick film process development

The effects of reflow were exacerbated by using thicker films and ultimately limited our ability to fabricate thicker mechanical structures. This is shown in Figure 3, where AZ 9260 was used in an attempt to form thicker features. The film was patterned before pyrolysis. The image shows the rounded shape of the cantilevers after the pyrolysis process. The reflow process resulted in a complete loss of dimensional control.

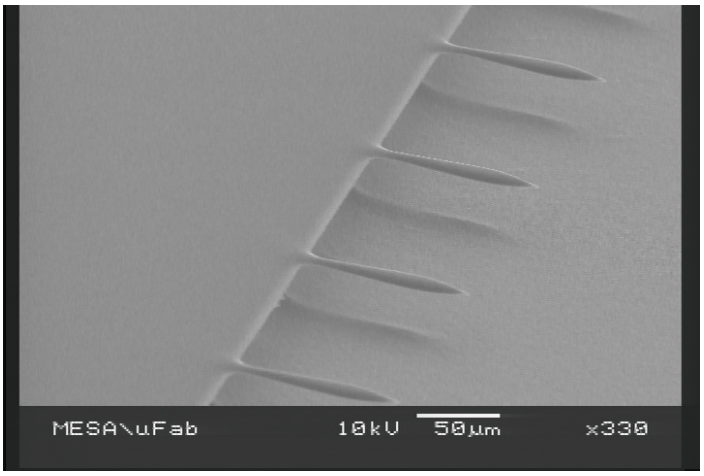

Figure 3: Cantilevers fabricated out of AZ 9260 photoresist. The features were patterned prior to pyrolysis.

To prevent the structures from rounding at elevated temperatures, a process was developed where blanket films were first pyrolyzed, then etched to define features by using a reactive ion etch (RIE) process. Pyrolyzed carbon is relatively difficult to etch and a high degree of ion bombardment is required. Best results were found by using a fluorine-oxygen chemistry. Since this chemistry etches common hard masks such as silicon oxides and nitrides, thick films were required to pattern the carbon features. A higher selectivity alumina hard mask was successfully demonstrated during the project. This was deposited by electron beam evaporation and patterned

using a lift-off process. Cantilever beams patterned by RIE after the pyrolysis process are shown in Figure 4. It is apparent from the SEM that the sidewalls are now vertical.

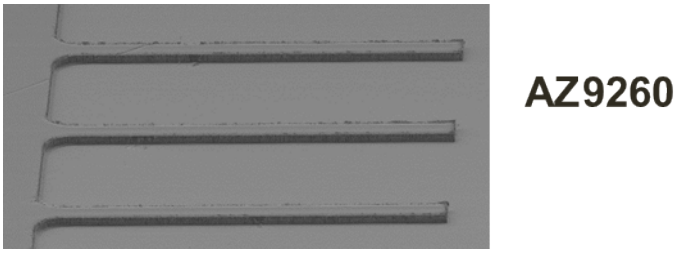

Figure 4: Cantilevers patterned by RIE after pyrolysis.

The structures were fabricated in a single layer on SOI wafers and dry released in XeF_2 gas. 50 XT photoresist was spin deposited 1300 rpm to achieve >50µm thick pre-pyrolyzed blanket film. After pyrolysis the PPR was patterned using RIE and a SiO_x hardmask. The thickness of the carbon after pyrolysis was measured using a SEM and found to be 7.8µm. The SEM images in Figure 5 show features that are clearly defined with reasonably vertical sidewalls. This is the thickest, high quality film we fabricated during the project. The downward curvature of the cantilever structures shows that they have a slight compressive stress gradient. As discussed earlier, it ultimately proved difficult to reproduce these results, which was believed to be caused by uncontrolled variables in the smaller furnace.

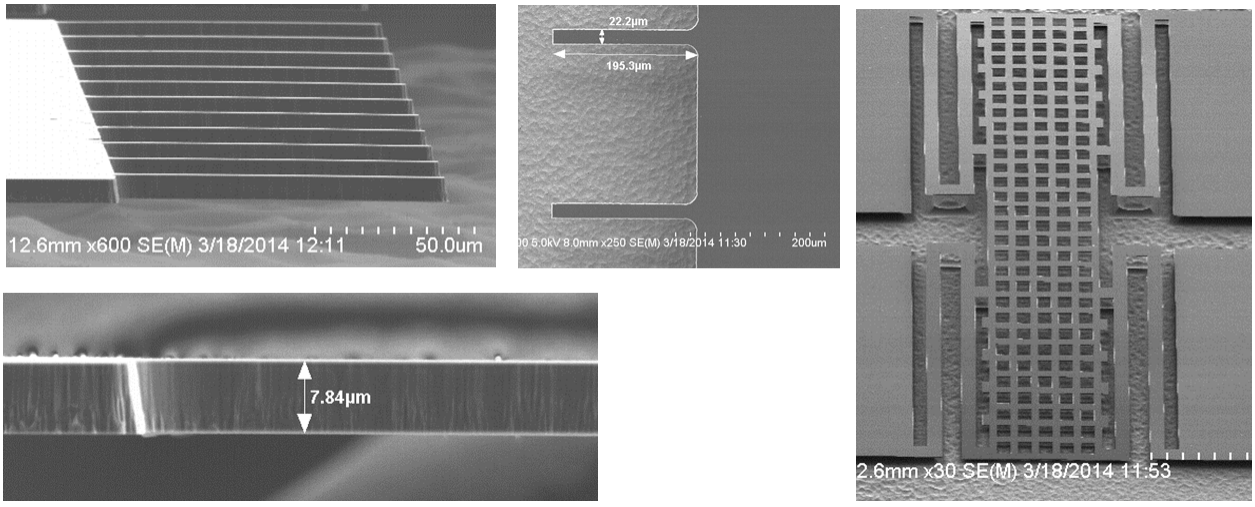

Figure 5: SEM images showing a demonstration of a thick-film process using pyrolyzed 50XT photoresist. The film thickness is almost 8µm thick and the features for formed by etching the carbon after the pyrolysis process.

2.4 Volume-scalable fabrication processes on 6-inch diameter wafers

Two novel multi-layer processes were developed on 6" diameter Si wafers: (1) carbon-on-SUMMiTV™ and (2) carbon-on-carbon. Both processes were motivated by the need for an electrically conductive layer for routing drive and sense signals. The primary challenge with a two layer process is the high pyrolysis temperature of the carbon mechanical layer. It proved difficult to find a metal that could withstand the process without peeling or reacting with carbon.

The SUMMiTV™ surface micromachining process is ideal because it already sees these temperatures during the course of processing, and chemical mechanical polishing is used to planarize the topography at each layer. It is a 5-level polysilicon surface micromachining process fabricated on 6" diameter wafers in the Microelectronics Development Laboratory (MDL) at Sandia. Although, in theory, all 5 layers could have been used, we demonstrated the process by fabricating PPR mechanical structures on the electrical signal layer (poly0). PPR is also ideal as a signal routing layer. The material is conductive and it is compatible with the high-temperature pyrolysis process. Furthermore, by using polySi as the sacrificial material, an all-dry release is still possible using XeF_2 gas.

The pyrolysis process was moved to a furnace located in Bldg. 878. This furnace accommodates multiple 6" diameter wafers in a single run. In this system, the photoresists are pyrolyzed in a reducing ambient of pure H_2 flowed at a rate of 10 liters/minute. The temperature is linearly ramped at 5°C/min to 1050°C, held at 1050°C for 1 hour, then actively cooled at a rate of 5°C/min. In contrast to the smaller furnace in bldg. 701, the PPR films produced in 878 were consistently smooth and well adhered to the substrates, regardless of the pre-pyrolysis conditions.

2.4.1 Carbon on SUMMiTV™ process

A diagram of the process is shown in Figure 6. The wafers were processed through the first sacrificial layer in the MDL. Because of the production capability in the MDL, 24 wafers were fabricated in parallel using well-characterized processes. A new set of masks was generated for this process and care was taken to insure a smooth transition between the MDL, which uses stepper photolithography, and the Microfab, where we used contact aligners. The Si substrates were electrically insulated with a layer of low-stress silicon nitride deposited by low pressure chemical vapor deposition over a layer of thermally-deposited SiO_2. Next, a layer of heavily-doped polysilicon (poly0) was deposited and patterned by RIE to act as the electrically conductive layer. A sacrificial layer of SiO_x was deposited over poly0. Patterned openings in the sacrificial layer acted as anchors for the carbon mechanical structures. After this part of the process was completed, the wafers were transferred to the Microfab for further processing using the techniques previously described. A layer of 50 XT photoresist was spin deposited at 3000 rpm onto the wafers. The wafers were then pyrolyzed in bldg. 878, and returned to the Microfab for further processing. Mechanical features were defined using RIE and a SiO_x hard mask. The structures were released in a hydrofluoric acid bath that selectively etched away the oxide film, and dried in supercritical carbon dioxide. The final carbon thickness was approximately 4.4µm.

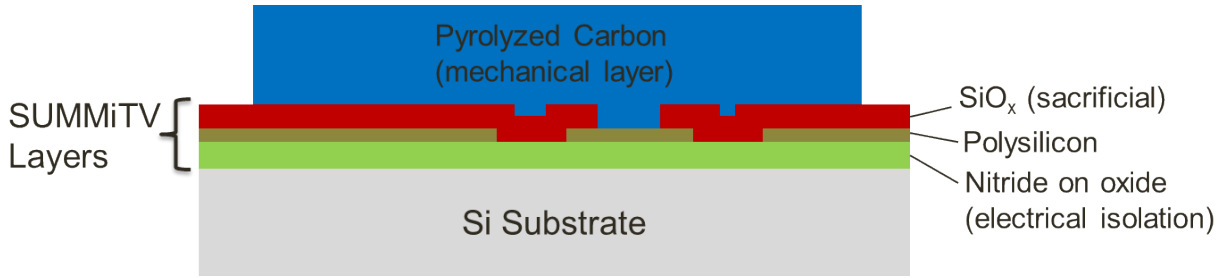

Figure 6: Carbon on SUMMiTV process. The cross-section shows a layer of pyrolyzed carbon over the first few layers of the SUMMiTV surface micromachining process. SUMMiTV is compatible with pyrolyzed carbon because it has similar high-temperature processes.

Representative SEM images of processed structures are shown in Figure 7. Several proof-of-concept mechanical structures were demonstrated. Upon inspection, the films appeared to be smooth with no evidence of blistering or cracking. There was a slight residual compressive stress gradient and a net compressive stress, which was typical for almost all of the PPR films in this project.

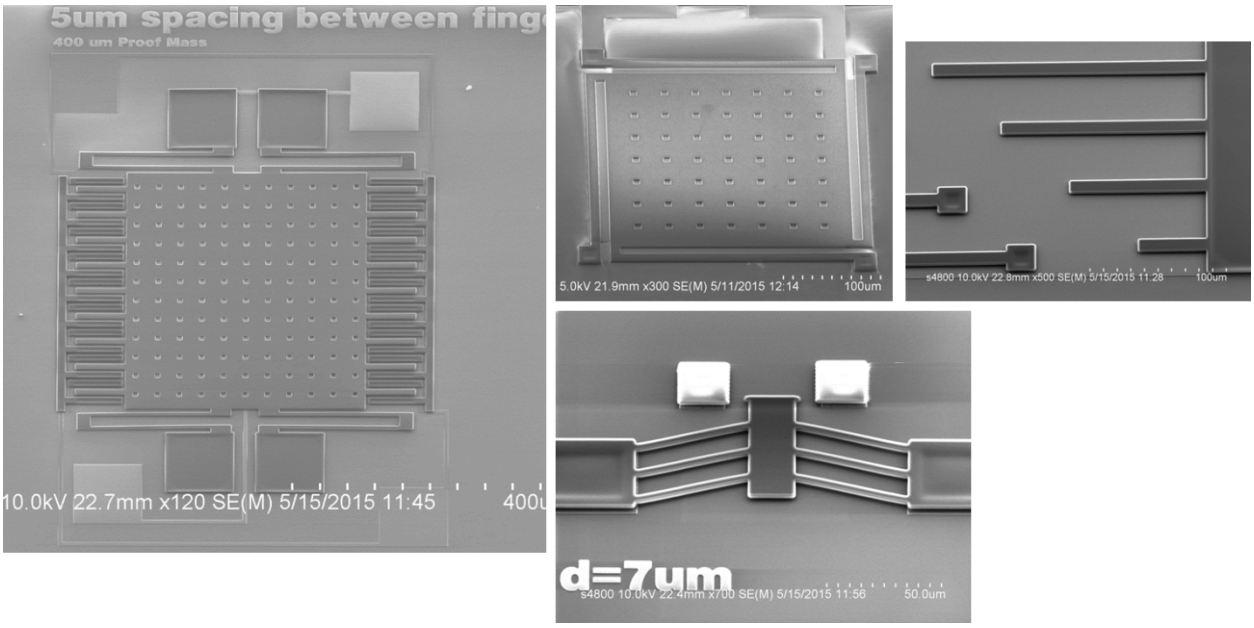

Figure 7: SEM images of carbon structures fabricated using the carbon-on-SUMMiTV process.

We noted that a number of the carbon mechanical structures were damaged as they were inspected by the SEM. The effect was dependent on the incident electron energy. More damage occurred at higher energies and less occurred at lower energies (approx. 1keV). This was attributed to the build-up of an electrostatic surface potential caused by the incident electrons. An example of a damaged structure is shown in Figure 8. The lower-magnification image on the lower left shows an area with a missing proof mass. Upon closer inspection (top and right images), the anchor regions appear to be rough and pitted around the edges with possible presence of nanowire structures. To examine this more closely, an unreleased sample was cross-section by focused ion beam (FIB) through an anchor. The SEM images in Figure 9 show that the mechanical PPR layer is separated from poly0 and the sacrificial layer at the edges of the bond pad. There are nanowires present in the gap and polysilicon has been consumed, which may account for the observed pitting, presumably during nanowire formation. This accounted for the poor adhesion of the carbon structures.

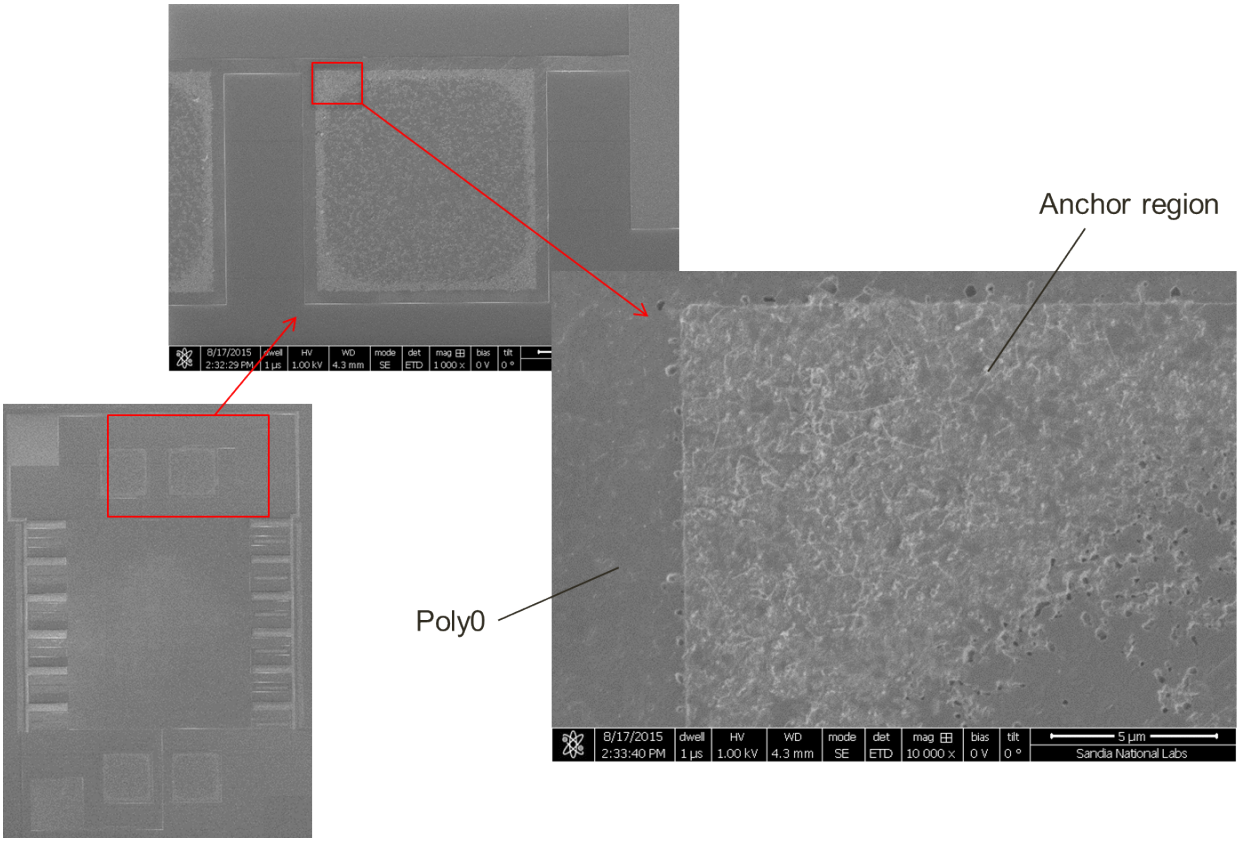

Figure 8: SEM images showing an inertial mass that lifted off during the release process. The high-magnification image on the right shows the exposed area where a carbon bond pad lifted off. Pits, roughness, and nanowire structures are evident.

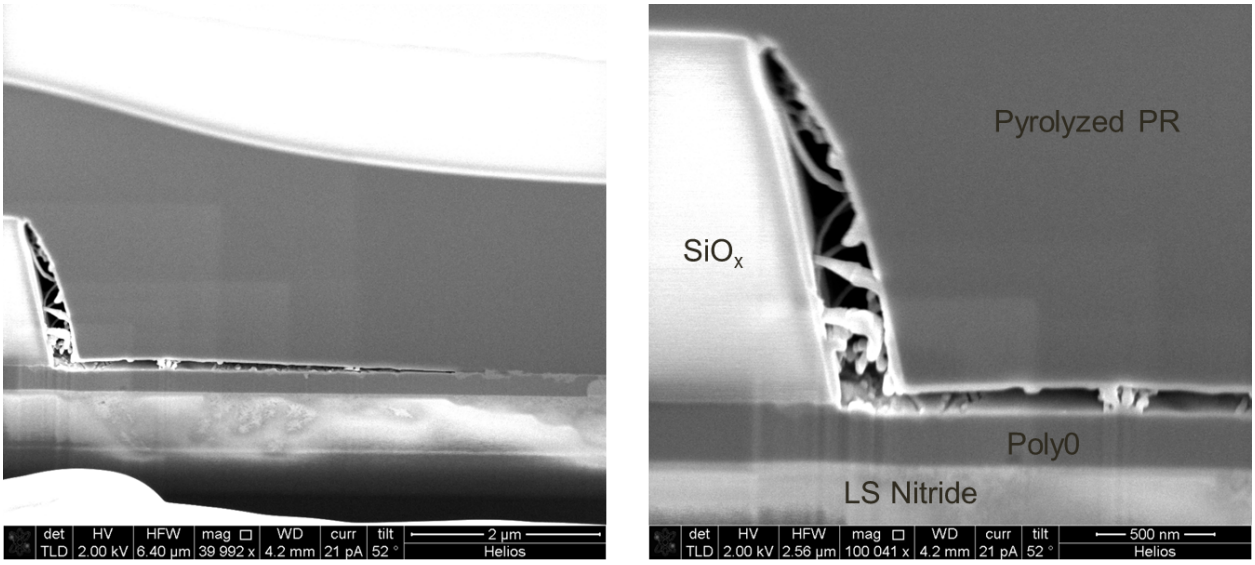

Figure 9: FIB cross-sections of the edge of an anchor region. Separation is evident prior to the release process. The formation of silicon nanowires may account for the observed separation at the carbon-poly0 and carbon-SiO_x interfaces, and pitting in the polysilicon layer.

2.4.2. Carbon-on-carbon process

A diagram of the process is shown in Figure 10. The same starting material was used here that was used in the previous process: 6" diameter wafers covered with insulating layers of SiN over SiO_2. In the Microfab, a layer of pyrolyzed carbon was spin coated over the wafers. The wafers were pyrolyzed in bldg. 878, and returned to the Microfab to be patterned by RIE. A polysilicon sacrificial layer was then deposited by LPCVD and patterned by RIE. A thicker layer of 50 XT photoresist was spin deposited at 3000 rpm and subsequently pyrolyzed in bldg. 878. The pyrolyzed carbon was patterned using RIE and an oxide hard mask in the Microfab. The structures were released in XeF_2 gas.

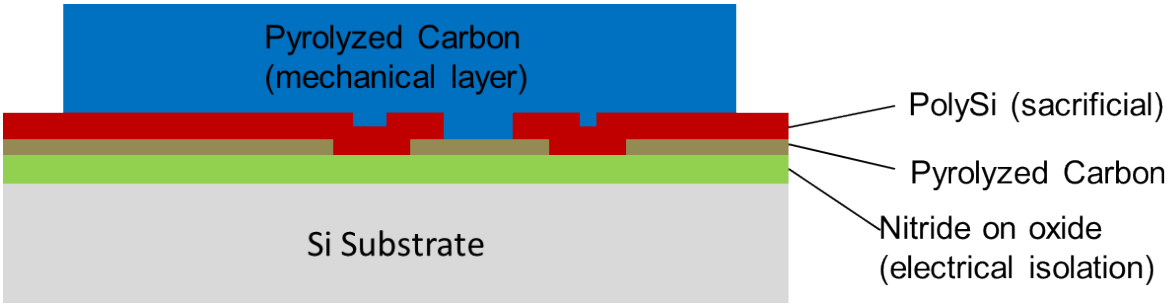

Figure 10: Carbon-on-carbon process. The cross-section shows a mechanical layer of pyrolyzed carbon over a conductive (non-mechanical) layer of pyrolyzed carbon. Polysilicon was used as the sacrificial layer. This was removed by selective XeF_2 etching.

SEM images of the released structures are shown in Figure 11. Again, the films appeared to be smooth with no evidence of blistering or cracking, and again there was a characteristic residual compressive stress gradient and net compressive stress. These structures were well-adhered to the substrate.

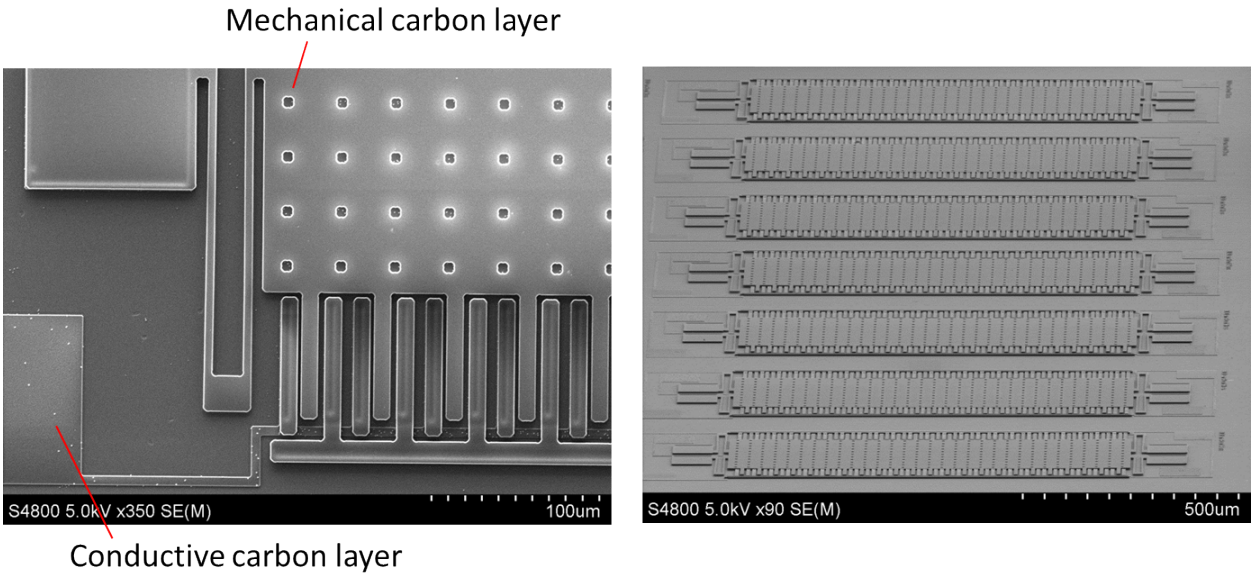

Figure 11: SEM images of released structures fabricated using the carbon-on-carbon process.

In general, the films were significantly affected after the release process by net compressive stress. Analysis of the buckling of clamped-clamped beam structures provides an approximation of this value. Figure 12 shows a scanning white light interferometry rendering of an array of bridges starting at 50µm length and increasing in 50µm increments. Eight arrays were imaged and the results are summarized in the table accompanying the figure. All of the bridges above 50µm are buckled because of residual compressive stress. Application of the Euler buckling formula results in a calculated compressive stress range of 16 to 63MPa. This calculation overestimates the amount of residual compressive stress, as the beams are not ideally clamped-clamped beams. The anchors are compliant and the resulting asymmetry will preferentially buckle the beams in a direction away from the substrate. Although it was deemed to be of secondary importance to this work, more rigorous modeling of the anchor by finite element modeling gives a more accurate compressive stress value.

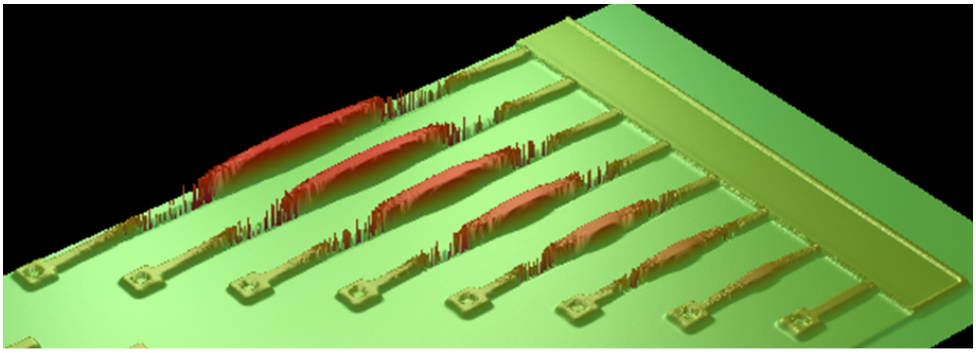

Array name	Longest unbuckled length	Shortest buckled length	Lower Bound	Upper Bound
CC 01	50	100	1.57E+07	6.26E+07
CC 02	50	100	1.57E+07	6.26E+07
CC 03	50	100	1.57E+07	6.26E+07
CC 04	50	100	1.57E+07	6.26E+07
CC 05	50	100	1.57E+07	6.26E+07
CC 06	50	100	1.57E+07	6.26E+07
CC 07	50	100	1.57E+07	6.26E+07
CC 08	50	100	1.57E+07	6.26E+07

Figure 12: A scanning white light interferometry image showing an array of clamped-clamped beams 10µm wide ranging from 50 to 400µm long in 50µm increments. Only the 50µm beam was not buckled for all 8 arrays. The table shows the corresponding critical buckling stress range (in Pa) calculated for 8 identical measured arrays.

We did not calculate the residual compressive strain gradient, however the amount of downward deflection was measured on a number of cantilever beams by scanning white light interferometry. A representative result is shown in Figure 13. The approximate deflection is 0.8µm per 100µm long beam.

The strain gradient was altered by the presence of the oxide hard mask. Before the oxide layer was removed (following the RIE process to pattern the carbon layer), the strain gradient of the composite carbon-oxide structure was pronounced and tensile. Once the oxide was removed, the gradient reverted to being slightly compressive. This suggests the possibility of controlling the residual strain gradient by either depositing or leaving an oxide film of a specified thickness on top of the carbon.

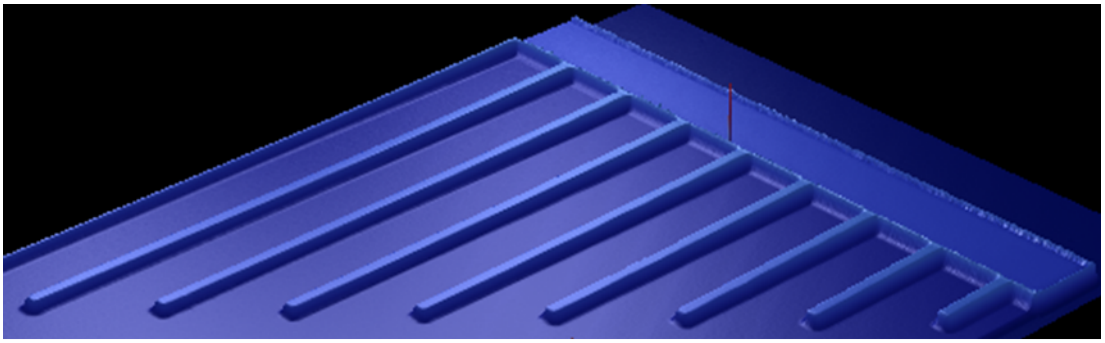

Die Name	Beam Length	Deflection	Radius of Curvature [m]
Rebus 1	129	1.17	0.01
Rebus 2	136	1.12	0.02
Rebus 3	139	1.12	0.02

Figure 13: A scanning white light interferometry image showing an array of cantilevered beams 10μm wide ranging from 50 to 400μm long in 50μm length increments. The measurements of a 150um long cantilever from 3 different arrays from the same 6" wafer are summarized in the table.

3. CHARACTERIZATION OF UNLOADED PPR FILMS

3.1 Nanoindentation Analysis

Three samples of pyrolyzed AZ 50XT photoresist were measured by Tom Bucheit in Bldg. 701 using a Berkovich diamond indenter. The photoresist was spin deposited at 3000 rpm to f thickness of >30µm. The samples were indented to a depth of 250nm. Sixteen indents were made at each depth increment. The hardness and Young's modulus were calculated from the indentation measurements and are plotted in Figure 14. The average hardness and modulus calculated over a depth of 100 – 200nm are summarized in Table 2. The modulus varies from 22.0 to 23.4GPa and the hardness ranges from 3.8 to 4.2GPa.

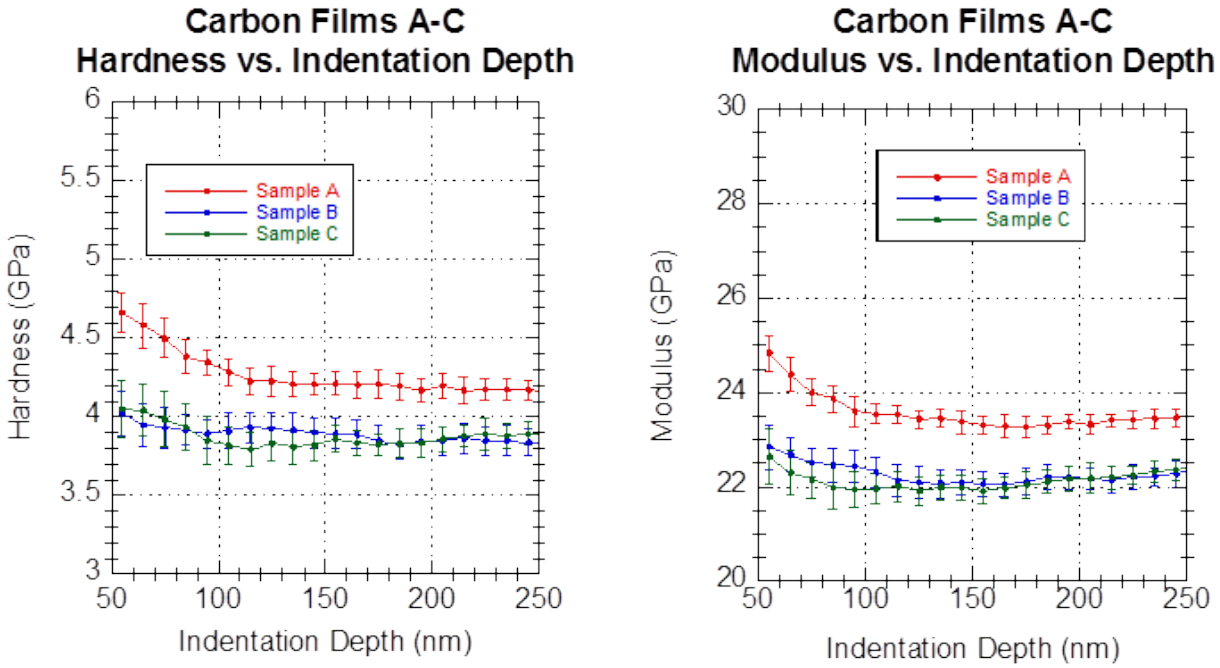

Figure 14: Indentations of Samples A, B, and C to 250nm depth.

Table 2: Nano indentation results (250 nm depth)

Averaged results for 100-200nm				
Sample	Hardness (GPa)	Std. Dev.	Modulus (GPa)	Std. Dev.
A	4.22	0.042	23.407	0.11
B	3.894	0.077	22.142	0.239
C	3.825	0.073	22.003	0.222

Young's modulus values were also extracted by means of measuring the frequency response of patterned micro-cantilever structures. A value of 41 GPa was measured for pyrolyzed AZ 4330 films, as detailed later in Section 4. We did not investigate the discrepancy between this value and the value measured using nanoindentation.

3.2 Temperature Coefficient of Resistance

Measurement of the temperature coefficient of resistance (TCR) of the pyrolized carbon films was made using several varieties of the carbon parts mounted on a 24-pin ceramic DIP package.

Since the devices were mounted in the DIP packages with the lids removed, the experiment was conducted in a 2" diameter tube furnace (Thermodyne Type 21100) with a small (~100 SCCM) flow of house N_2 passing over the devices to purge the O_2 from the vicinity of the carbon to prevent oxidation of CO_2 at elevated temperatures. The experimental arrangement is shown in Figure 15. The parts were then tested at temperatures over a range of ambient (~23C) to above 500C. Since electronic solders melt at around 200C, 30 AWG soft-Ni-coated Cu "wire-wrap" wire was spot welded onto the BeCu (Beryllium-Copper) pins of the ceramic DIP packages to prevent loss of electrical conductivity at high-temperatures due to solder melt. This was accomplished by using a Miyachi/Unitek Model 250 Dual Pulse micro-spot welder. The wires were welded such that two ~24" bare wires were attached to each pin allowing a 4-wire resistance measurement that eliminates temperature effects from the long connection wires (see Figure 15). The devices were then suspended in the center of the tube furnace by using a 12" long piece of machined ceramic with 4 axial holes to provide both electrical isolation and provide mechanical support.

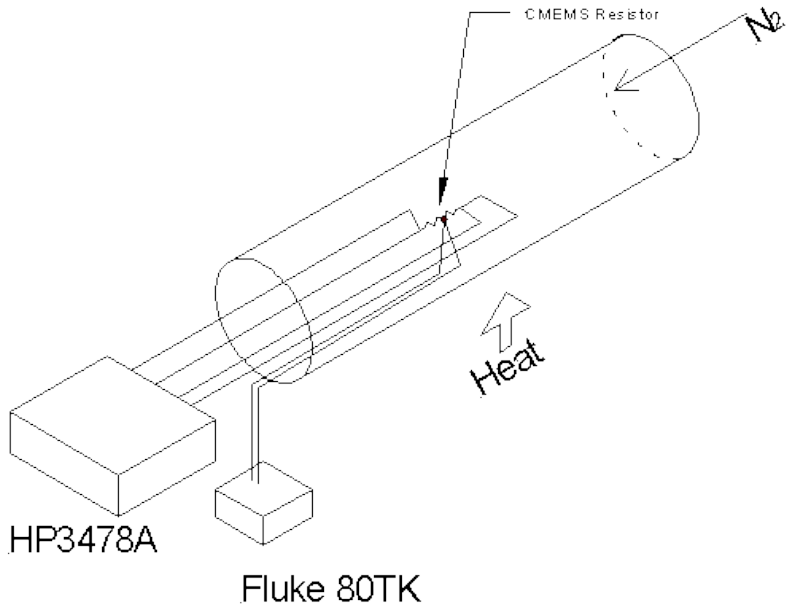

Figure 15: Diagram of the measurement system showing the tube furnace and the measurement hardware.

Electrical measurements were made by using an HP-3478A model digital ohm meter configured to operate in 4-wire ohms mode. The resistance was then measured as a function of temperature by cycling the system several times from room temperature to 500 C and recording the data. The temperature of the component was measured by placing a type "K" thermocouple attached to a Fluke 80TK thermocouple linearizer to a digital voltmeter and placing the thermocouple in close proximity to the ceramic DIP package. Temperature ramping was conducted at a slow rate (~1C/sec) that assured quasi-static conditions such that the ceramic package and the thermocouple were at the same temperature in the tube.

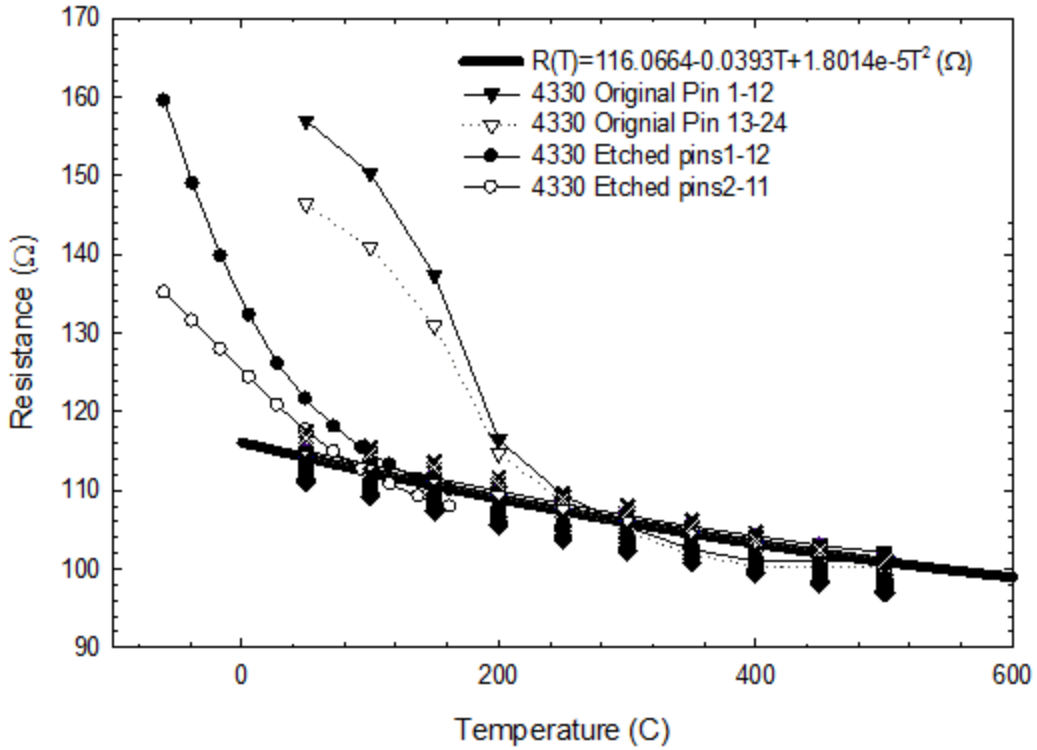

Figure 16: The data plotted above is the resistance vs. temperature for two types of material (4330 Original and 4330 Etched). Data illustrate several temperature cycles of the material. Initially, the resistance starts high (~150Ω) and then drops as the temperature rises. This is due to the desorption of the H_2O. On subsequent temperature cycles this does not repeat due to the constant background of N_2 around the parts. The solid-black line is a quadratic fit of the stabilized data as a function of temperature.

The response of the carbon resistor structures was then measured and is plotted in Figure 16, which is a plot of the resistance of the structure as a function of temperature. Four separate carbon MEMS resistors were measured from two separate substrates. These samples were two 4330 Etched samples and two 4330 Original samples prepared as described above. The data with the circles is the initial response from the 4330 Etched parts the first time the devices were heated and measured. Likewise, the inverted triangles are the response from the 4330 Original parts the first time the devices were heated and measured.

In all the cases, the resistance is initially on the order of 130 Ω to 160 Ω prior to heating. The resistance then drops in all cases to 115 Ω ± 5 Ω at 0C after heating. The devices can then be cycled from room temperature to above 550C along the contour shown in the plot without the resistance returning to the initial value as long as the device is kept under a constant dry N_2 atmosphere. If the device is removed and set in an air ambient for an extended period greater than 2 days, the resistance will return to approximately the same initial value of 130 Ω to 160 Ω and the process will repeat on initial heating. We postulate that ambient moisture absorption into the film is the origin of this effect. When the temperature is raised above 200C, the moisture is

driven out of the film and the resistance is reduced. Likewise, exposure to ambient air causes the resistance to increase requiring a bake-out prior to temperature cycling.

As the plot demonstrates, the resistance of all of the parts converges and repeats as a function of temperature. Ignoring the initial conditioning data, all of the temperature stabilized data was fitted to find the quadratic function shown in the thick-solid line (rounded to two significant figures). The data fit results in the following parameters:

$$R(T) = 120\,\Omega - 0.040\ \Omega/^{\circ}C\ T + 1.8\times10^{-5}\ \Omega/^{\circ}C^{2}\ T^{2} \quad \text{(1)}$$

There are several points that are important about the coefficients of Eq. (1). First, the coefficient of the quadratic term is very small compared to the other terms indicating that the response ofthe material is very nearly linear over the entire range of temperatures. Next, the constant term (120Ω) is a parameter that is controlled by the manufacture of the parts and can be set to values of the designer's choosing. Our parts are consistently in the range of 115 Ω ± 5 Ω at 0 C.

From the definition of resistivity ($\rho(T)$) for a part that is 1.5 μm thick, 200 μm wide, 800 μm long and has a resistance of 120 Ω at 0C:

$$\rho(T) = \frac{A}{l}R(T) = \frac{200\mu m \cdot .5\mu m}{800\mu m}\cdot 20\Omega = 4.5\times10^{-5}\left[\Omega - m\right] \quad \text{(2)}$$

$$\frac{d\rho(T)}{dT} = \frac{A}{l}\frac{dR(T)}{dT} \approx -0.040\ \Omega/^{\circ}C\ \frac{A}{l} = -1.5\times10^{-8}\left[\frac{\Omega - m}{K}\right] \quad \text{(3)}$$

R(T) is the measured resistance, *A* is the cross-sectional area of the structure, and ℓ is the length of the structure, we can infer the resistivity of the material to be approximately 3 to 8x10^{-5} Ω-m for all of our device geometries. This is consistent with other literature values reported for glassy carbons which are between 0.3x10^{-5} Ω-m to 4x10^{-5} Ω-m [1-3]. The resistivity is known to be highly dependent on processing temperatures and conditions in these pyrolyzed films. We have tested several devices with different widths and lengths and have found that the values for TCR are constant over all our geometries.

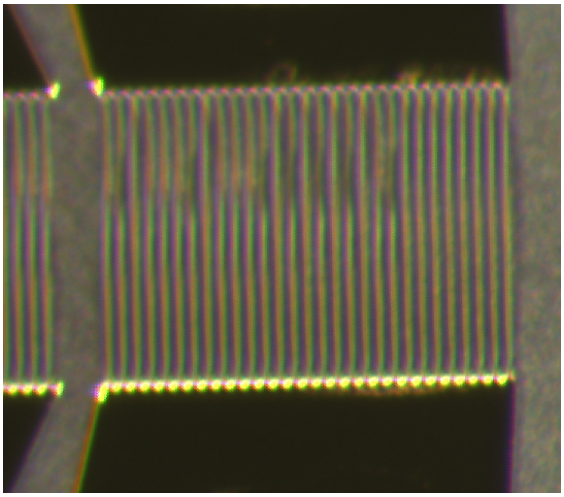

Figure 17: Photograph showing construction of the MEMS bridge structures. The 29 individual filaments are 10µm wide by 1.5µm thick by 400µm in length and are free standing with electrical contacts on the top and bottom of the structure in the photo.

If we take the derivative of Eq. * MERGEFORMAT (2), we can determine the temperature coefficient of resistivity from the linear coefficient in Eq. * MERGEFORMAT (1). This resistance change represents a thermal coefficient of resistance (TCR) of about -1.5×10^{-8} Ω-m/K for this material. This is consistent with values of temperature coefficient of specific resistivity found from the literature for these types of glassy carbons.[iv] Literature values for pyrolyzed carbon films formed under different conditions can vary significantly. For example, literature values of coefficient of specific resistivity found for bolometers produced from parylene-pyrolyzed carbon have values on the order of -2%/K indicating significant morphology differences between the two materials [4,5]

3.3 CMEMS Bridge Temperature

An additional CMEMS structure was constructed by forming the material into free-standing bridge arrays with individual filaments of 10 µm width, 1.5 µm thickness, and 400 µm length. An example of these devices is shown in Figure 17 which shows a single bridge structure with 29 individual filaments wired in parallel to two Au bond pads on the top and bottom of the structure. Measurement of the device temperature was made by using a Optotherm Sentris Infrasight MI320 model thermal imager and a Keithley model 2400 source meterto provide the current. Thermal images of the bridge array were then taken and analyzed to determine the maximum temperature of the device as a function of the input voltage and current. An example of this type of data on a bridge structure is given in Figure 18.

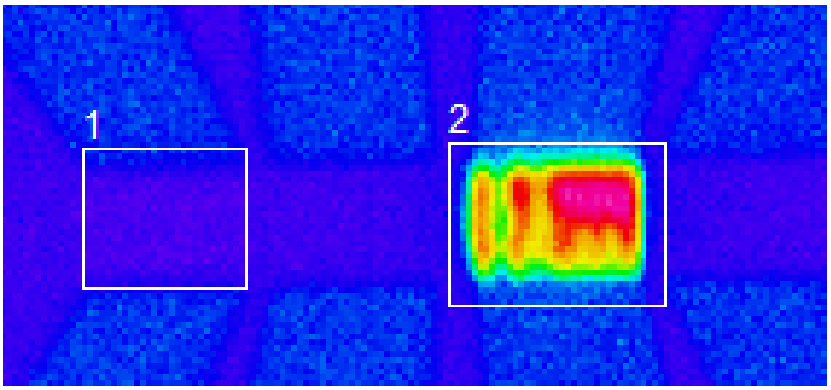

Figure 18: Thermal graph of one bridge array electrically heated. The maximum temperature is 33.9C in this example. Box 1 is measured to get an ambient temperature background and box 2 is the heated array. Note several bridge filaments are missing in this array demonstrating the spatial resolution of the measurement.

Figure 18 is a thermal graph of the temperature on one set of the four bridges on the substrate labeled box 2. The region surrounded by box 1 is for measurement of the ambient temperature of the substrate and allows an accurate measurement of the maximum temperature of the filaments. In the photo the magenta colored area has the highest temperature above background (blue). In addition, in this measurement, several filaments were burned out as indicted by the green and yellow regions of the photo. This provides an estimate of the spatial resolution of the measurement instrumentation.

Measurements of the current as a function of voltage were taken over a wide range of temperatures and for multiple devices and were compared to the temperatures measured. These data are plotted in Figure 19 which shows a series of cycles from 0 V to 7.5 V in the tube furnace with an N_2 atmosphere to prevent oxidation of the carbon and destruction of the filaments. As is indicated by the data, the device can cycle between 0 and 200 mA of current multiple times without incurring permanent changes in the device behavior or reaching failure. The data represented by the blue squares is data acquired in the thermal imager where there is N_2 flowing over the device, but the device is otherwise exposed to the atmosphere. Thus, the thermal imager has less precise control over the oxygen concentration above the device.

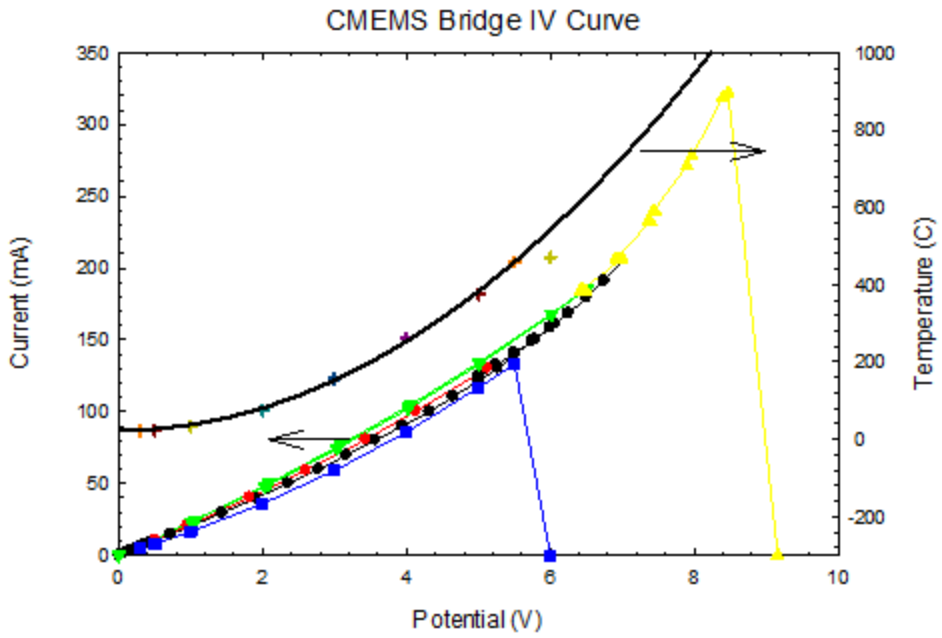

Figure 19: Plot of current vs. applied potential to several different MEMS bridge structures measured over several cycles in the tube furnace. All data sets except the blue squares and the yellow triangles were made without driving the device to destruction. In the case of the yellow squares, the device is driven to failure in the N_2 atmosphere of the tube furnace and in the case of the blue squares; the device is driven to failure in the thermal imager which has less precise control of the O_2. The solid-line fit to the crosses is the corresponding temperature measured in the thermal imager as a function of potential. The data are fit to a quadratic model developed below.

The corresponding temperature is plotted for the data from the thermal imager (blue squares) showing the maximum temperature as a function of voltage. It is observed that the maximum measured temperature is 490 C which is the saturation value of the thermal imager. We have fitted the data to a quadratic function to allow extrapolation of the temperature at the currents possible in the non-oxidizing atmosphere (N_2) of the tube furnace. This is plotted as the solid (Figure 19) black line. The extrapolation indicates that under inert conditions, the devices can reach 1000 C prior to failure.

A series of experiments were conducted that included operating a device in the non-oxidizing atmosphere to 7 V in the tube furnace to characterize its performance without driving it to failure and then transferring that device into the thermal imager to compare its response while intentionally driving that device to failure. These data are plotted in Figure 20 and show the device current as function of drive voltage and the corresponding temperature of the device as measured by the thermal imager. In the data acquired in Figure 20, the voltage was only turned on for approximately 0.5 sec in order to reduce the burn-out of the filaments. Thus, the current data in the thermal imager begins to become smaller at 5 V and continues to drop as the voltage is increased until all of the filaments are destroyed. The corresponding temperature decrease is also observed and plotted above 5V.

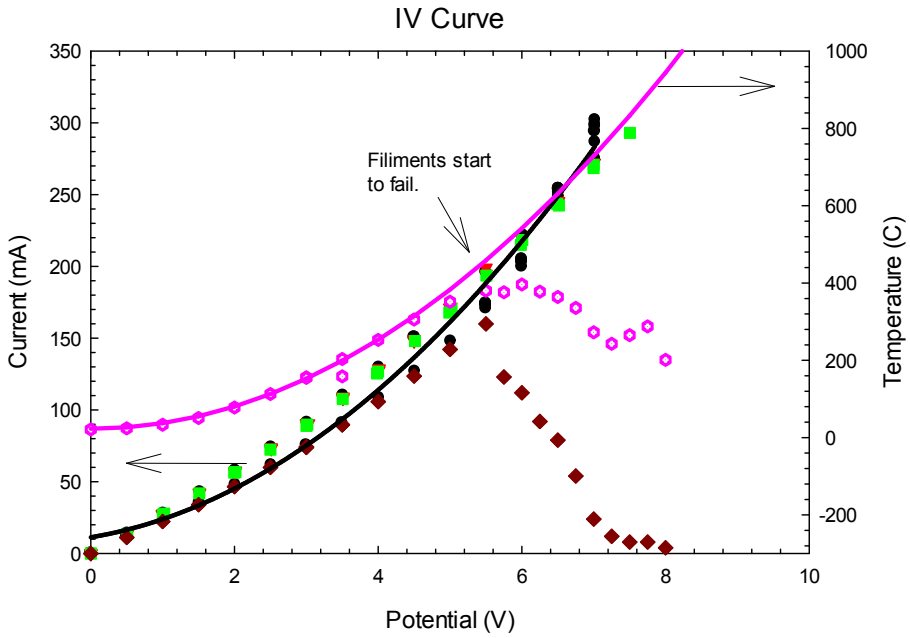

Figure 20: Plot of current vs. applied potential to a MEMS bridge structure measured over several cycles in the tube furnace. All data sets except the dark red diamonds were made without driving the device to destruction. In the case of the red diamonds, the device is driven to failure in the N_2 atmosphere of the thermal imager. The data are fit to a quadratic model (solid magenta line).

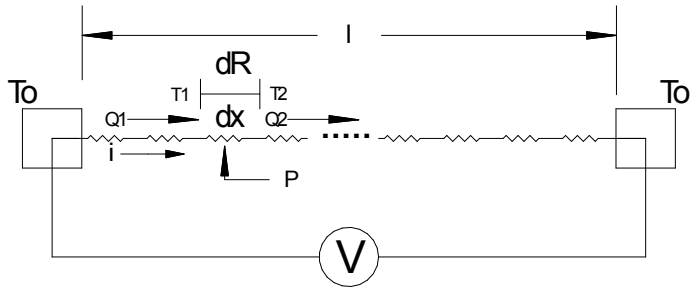

Figure 21: Notional diagram of CMEMS bridge connected at each end with a thermal reservoir at *To*. Each differential length of the carbon filament can be thought of as an individual resistor with a constant current.

Figure 21 is a thermal model of the carbon bridges that a tied at either end at a constant temperature (T_o) reservoir. The bridge can be thought of a series of individual resistors with differential length dx and differential resistance dR. The heat flowing from the left-hand side into the resistor is Q_1 and the heat flowing out of the differential element of resistance is Q_2. These nodes are at temperatures T_1 and T_2 as illustrated in Figure 21. If we consider the conservation of energy across the differential element of resistance, we recognize that the heat flowing into the element from the adjacent element plus the electrical energy dissipated in the element integrated over time with the heat flowing out of the right side subtracted must be equal to the product of the specific heat of the carbon (c_p), mass density of the carbon (ρ_m), cross-sectional area of the beam (A), and the length of the differential element of the beam (Δx) multiplied by the change in temperature. This is written mathematically as:

$$Q_1 - Q_2 + \int_0^t P(x,t)dt = c_p \rho_m \, A \, \Delta x \, \Delta T \qquad \text{* MERGEFORMAT (4)}$$

For the steady state case where the total resistance of the beam is static as occurs when the beam is heated to steady-state, Eq. * MERGEFORMAT (4) reduces to the following:

$$Q_1 - Q_2 + P(x,t)\Delta t = c_p \rho_m \, A \, \Delta x \, \Delta T \qquad \text{* MERGEFORMAT (5)}$$

Dividing by Δt and rearranging terms allows us to write the following form:

$$\frac{Q_1 - Q_2}{\Delta t} + P(x,t) = c_p \rho_m \, A \, \Delta x \, \frac{\Delta T}{\Delta t} \qquad \text{* MERGEFORMAT (6)}$$

In the limit of $\Delta t \rightarrow 0$, and $\Delta x \rightarrow 0$, Eq. * MERGEFORMAT (6) reduces to the following partial differential equation:

$$\frac{\partial Q}{\partial t} + P(x,t) = c_p \rho_m \, A \, \partial x \, \frac{\partial T}{\partial t} \qquad \text{* MERGEFORMAT (7)}$$

We now recognize that the term $\partial Q/\partial t$ for a uniform, homogeneous beam is the fundamental law of heat conduction [6]

$$-kA\frac{\partial T}{\partial x} + P(x,t) = c_p \rho_m \, A \, \partial x \, \frac{\partial T}{\partial t} \qquad \text{* MERGEFORMAT (8)}$$

Rearranging the terms of Eq. * MERGEFORMAT (8) and restricting our measurements to steady-state conditions ($\partial T/\partial t \rightarrow 0$), we can integrate over the length of the carbon filament as the following:

$$\begin{aligned} -kA\frac{\partial T}{\partial x} + P(x,t) &= 0 \\ kA \int_0^t dT &= \int_0^l P(x,t)dx \end{aligned} \qquad \text{* MERGEFORMAT (9)}$$

Again, invoking steady-state conditions and uniform homogenous materials, the power dissipated as a function of time and position is a constant P_o where Ohm's law provides a relationship between applied voltage (Figure 21) and power where R is the total resistance of a single filament.

Thus, Ohm's law leads to a substitution for the electrical power dissipated in the beam allows us to solve for the maximum temperature of the beam as a function of the applied voltage:

$$T = T_o + \frac{l}{kRA} V^2 \qquad \text{* MERGEFORMAT (10)}$$

The data for a complete set of filaments was then fitted to Eq. * MERGEFORMAT (10) and plotted in Figure 19 (solid black line) and Figure 20 (solid magenta line). This model has the following form where V is the applied potential to the filaments. As noted, when the applied potential is zero the model predicts that the temperature will be ambient as required.

$$T(V) = 23C + 14.4\,C/V^2\,V^2 \qquad \backslash* \text{ MERGEFORMAT (11)}$$

Since we know the approximate values of the geometry for the beams, remembering that there are 29 bridges in parallel so the resistance of a single filament of one is 29 times greater than what is inferred from Figure 20, we can now use the fit, geometrical values of the beams, and Eq. * MERGEFORMAT (10) to estimate the value of the thermal conductivity of the beam material as 2.1×10^3 W/(m-K). This value is order of magnitude consistent with other graphene and carbon nano-tube values reported in literature [7,8].

3.3 TEM Analysis

Transmission electron microscopy (TEM) was used to examine the structure of the pyrolyzed carbon material. Samples were initially prepared at Sandia using a focused ion beam (FIB) system to "cut" out a thin cross-section of one of the resistors fabricated out of AZ 4330, however the FIB process adversely affected the sample. A second sample was sent away to Evans Analytical for preparation by wedge polishing. According to the documentation slides generated by Evans Analytical, the sample was prepared for TEM by wedge polishing and broadband Argon milling, and the analysis was performed with an FEI Tecnai TF-20 instrument at 200keV beam energy. Dark field, bright field, high resolution imaging, and selected area electron diffraction analysis were performed on the samples. Some of the TEM images are shown in Figure 22 and Figure 23. In their report, Evans summarized the microstructure as largely amorphous with occasional small particles of crystalline carbon. Further analysis of the crystalline region produced results consistent with a graphite structure. The lateral dimension of the graphite structure in Figure 22 is greater than 0.5µm.

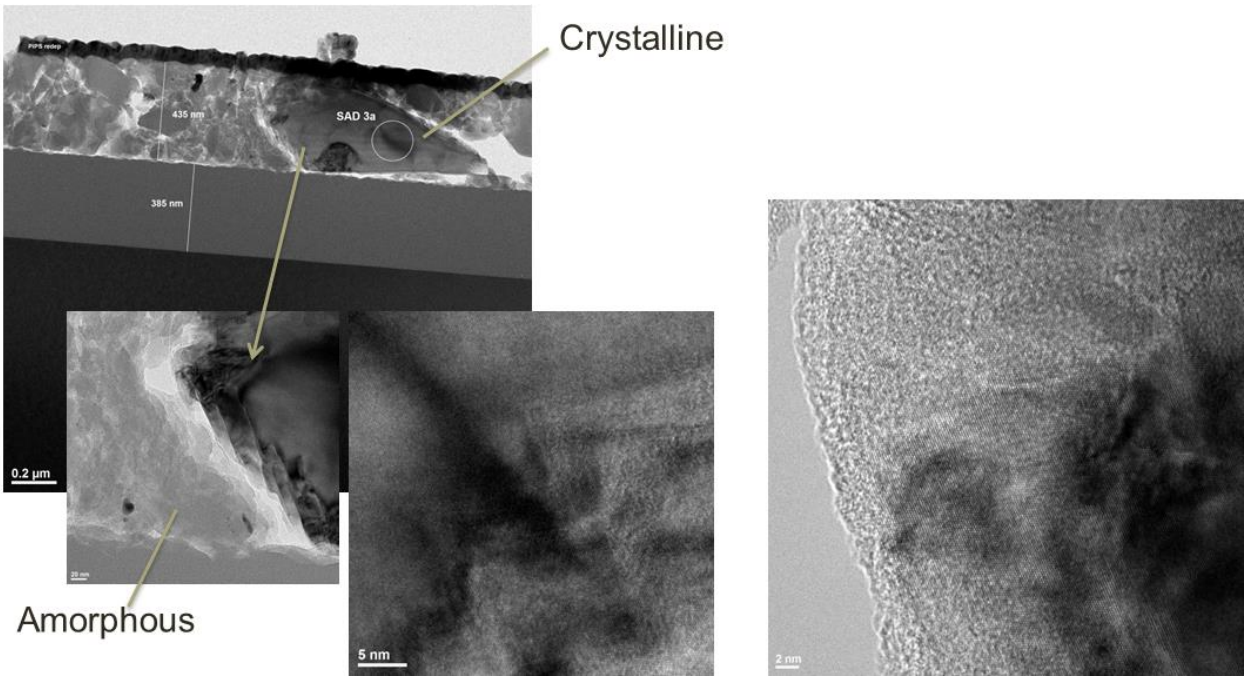

Figure 22: TEM images of pyrolyzed carbon on SiO_x on Si. The sample was prepared by wedge polishing. The two bright field images on the left side show an amorphous film with a prominent graphite crystal. The two high resolution mode images on the bottom and right show the transition between the crystalline and amorphous materials.

Other than to note the existence of graphite crystals in the film, we did not investigate them further (size, frequency, preparation dependency, etc…). The population of crystals was sparse and they were small relative to our mechanical geometries. This is apparent in the SEM image of Figure 24 where graphite crystals, visibly protruding from the sidewall of a broken cantilever beam, are both sparse and small relative to the size of the cantilever. At some point, an increase in the number of crystals or the use of smaller geometries could affect the homogeneous nature of the material and affect the mechanical, chemical, and electrical properties.

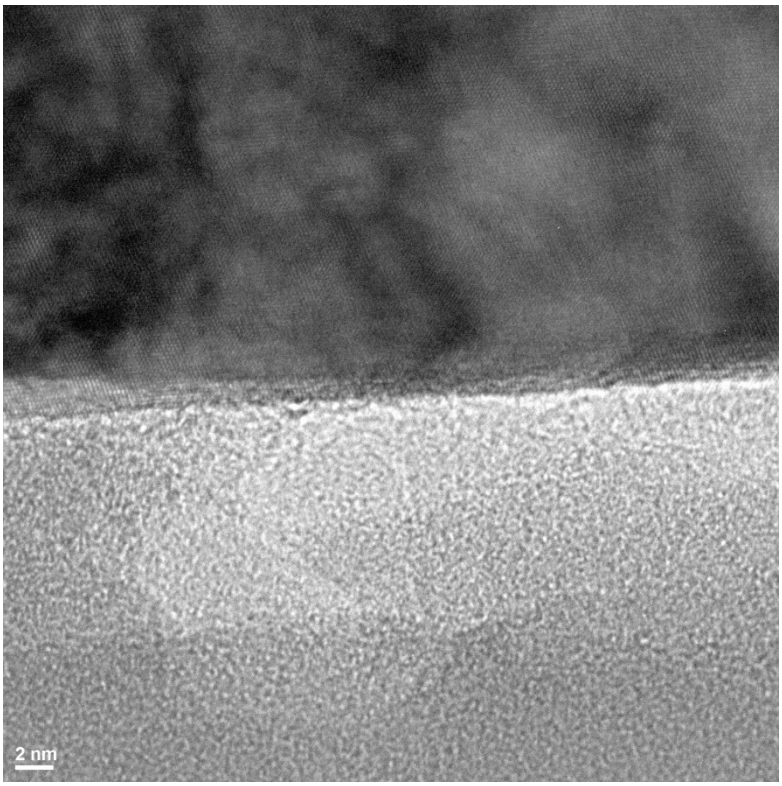

Figure 23: A TEM high resolution mode image showing the difference between the ordered atomic structure of the graphite crystal (top half of the image) and the disordered structure of the amorphous carbon region (bottom half of the image).

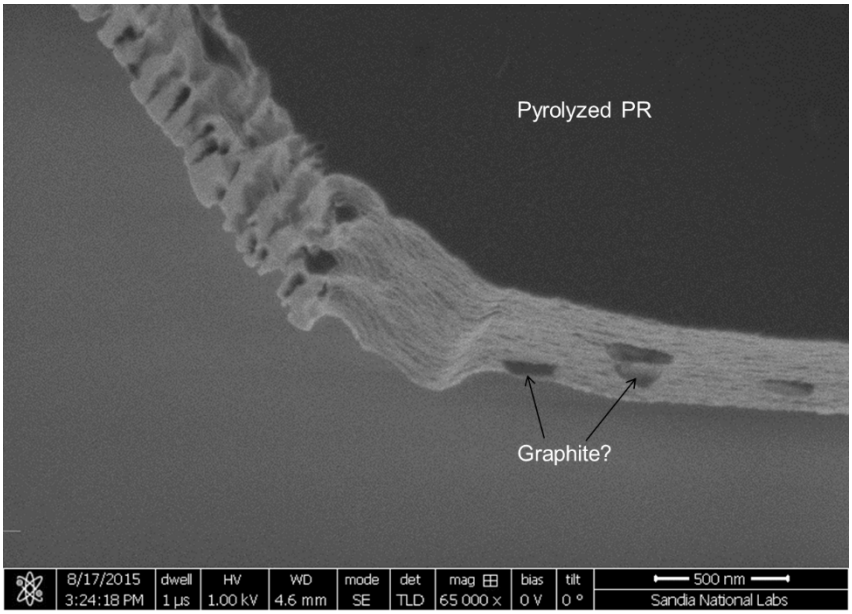

Figure 24: Side wall of a broken CMEMS beam showing possible locations of graphite crystals.

3.4 Density

The density of pyrolyzed AZ 4330 photoresist was measured using blanket coated 2-inch diameter silicon wafers. The mass of the bare wafers was measured using a microbalance with +/-0.1 mg accuracy. The mass was measured again after the AZ 4330 photoresist was spin coated and pyrolyzed. These two values were subtracted to obtain the mass of the pyrolyzed photoresist. The density was calculated using this value, the measured film thickness, and the area of the 2" diameter wafer. Density measurements of 1.25 g/cm^3 and 1.38 g/cm^3 were obtained in this manner. The results are summarized in Table 3.

Table 3: The mass measurements and density calculations of two pyrolyzed photoresist films.

Wafer #	PR Type	Bare Wafer Mass [g]	Wafer + PPR Mass [g]	Mass Change [g]	Film Thickness [µm]	Density [g/cm^3]
7	AZ 4330	1.3547	1.3585	3.80E-03	1.50	1.25
8	AZ 4330	1.3577	1.3619	4.20E-03	1.50	1.38

4. CHARACTERIZATION OF GRAPHENE LOADED PPR

Graphene nanomaterial and engineered resonators have been shown [15,16] to directly impact the Young's modulus and conductivity of the final material. In this section, we present evidence of graphene structure improving mechanical and electrical properties of pyrolytic carbon structures, suggesting unique carbon-carbon bonding arrangements due to the introduction of graphene which is still being understood.

Pyrolyzed photoresist containing iGO and iRGO was characterized using powder X-ray diffraction (PXRD), Raman spectroscopy, and elemental analysis. The conductivity of the loaded materials was measured using a 4-point probe. Young's modulus was calculated from laser Doppler velocimetry measurements of MEMS cantilevered beams. This information is summarized in [5]

An improved reduced graphene oxide (iRGO) was blended into pyrolytic carbon beams prepared for resonant frequency testing. Designed around a 10:1 (length: width) aspect ratio, the linearity of wt.% iRGO in the cantilevers as a function of resonant frequencies was evaluated. The collection of the 1st through 3rd bending modes using laser doppler velocimetry (LDV) of the graphene filled cantilevers shows an increase in frequency response with nanomaterial loading (wt.%). A model was developed using the 3-bending modes and correlated with cross sectional geometry and density to extract a Young's modulus.

4.1 iGO and iRGO materials analysis

4.1.1 Powder X-ray diffraction (PXRD)

Samples were mounted as EtOH slurries directly onto a zero background holder purchased from The Gem Dugout, State College, PA 16803 and allowed to dry. Samples were scanned at a rate of 0.02° / 2(s) in the 2θ range of 5−80° on a Bruker D8 Advance diffractometer in Bragg-Brentano geometry with Cu Kα radiation and a diffracted beam graphite monochromator.

iGO forms a well-ordered layered structure, as indicated by a well-defined d_{001} peak in its powder X-ray diffraction (PXRD) pattern. The exact 2θ values can range from 8-12°, depending on extent of hydration, and were determined to be ~ 2θ = 10.99° (correlates to a basal spacing of 8.08 Å) for the iGO samples prepared here, seen in Figure 25. The peak at ~ 2θ = 10-12° is lacking in the iRGO sample and the peak for the iRGO is observed at 2θ = 23.78° indicating a basal separation of 3.70 Å, larger than that of graphite at 3.35 Å. The broadness of the (002) peak is also consistent with poor ordering along the stacking direction and indicative of a powder comprised of disordered graphene-like nanosheets. The broad 101/001 peak(s) at 2θ = 42-44° suggests poor through plane alignment also consistent with a disordered material.

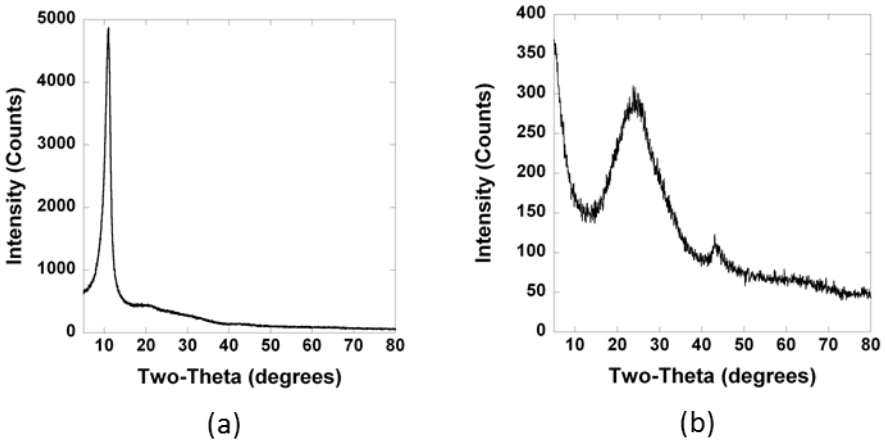

Figure 25: PXRD of the (a) iGO with peak at 10.99 ° and (b) iRGO with peak at 24° indicating disordered graphene-like nanosheets.

4.1.2 Raman Spectroscopy

Raman spectra were recorded using a Thermo Scientific Smart Raman DXR instrument with a DXR 633 nm laser with a high-resolution gradient from 150 cm^{-1} to 2100 cm^{-1}. Resulting data was analyzed using the Thermo Scientific software and re-plotted for presentation purposes using Kaleidagraph software.

The chemical reduction of iGO to iRGO [6] was also confirmed with Raman spectroscopy. The iGO as prepared here exhibits D- and G-bands at 1311 and 1594 cm^{-1} with a D/G ratio of 1.02. Upon hydrazine reduction, the G-band shifts from 1594 to 1586 cm^{-1}, while the D-band shifts from 1311 to 1336 cm^{-1}, as seen in Figure 26 (a) and (b). A marked increase in the I_D/I_G ratio of is also observed (I_D/I_G = 1.5). Shifts to lower wavenumbers are expected upon reduction and the accompanying increase in I_D/I_G ratio for RGO has been explained by the presence of smaller but more numerous sp^2 domains in the carbon [6].

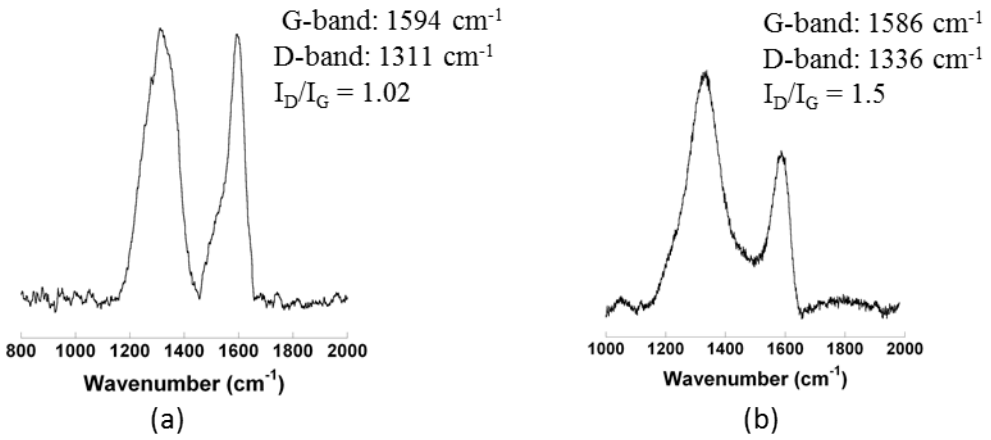

Figure 26: Raman Spectra for (a) iGO before the conversion to (b) iRGO upon hydrazine reduction.

4.1.3 Elemental Analysis

Elemental analyses were performed on a Perkin-Elmer 2400 CHN-S/O Elemental Analyzer. iGO and iRGO were analyzed for their C, H, N elemental composition. Values for the iGO prepared here are: 41.8% C, 55.8% O and 2.4% H. The iRGO elemental composition was found to be: 69.4% C, 23.8% O, 1.3% H along with 5.6% N, as seen in Table 4. The decrease in oxygen content is consistent with the chemical reduction of the graphene oxide. The presence on nitrogen in the iRGO is expected due to the N_2H_4 reducing agent [17].

Table 4: Elemental analysis of graphene materials.

Sample	C	H	O	N	C/O (EA)
Graphite	98.1	NA	1.9	-	51.6
iGO	41.77	2.44	55.75	0.04	0.749
iRGO	69.40	1.27	23.75	5.57	2.92

4.2 MEMS Design, Fabrication, and Characterization

4.2.1 Test Devices

The test devices used for this set of experiments are simple cantilevers of varying sizes that are affixed to bond pads, as shown in Figure 27. Both the cantilevers and the pads exist on the same layer and are comprised of the same material. Fillets at the base of the cantilevers serve to reduce mechanical stress at the joint between cantilever and pad. Several cantilevers of the same size share a single bond pad, and are placed along the edge of the pad with large spacing relative to cantilever width to minimize interference between devices.

All of the cantilevers, regardless of size, share the same thickness and a common aspect ratio of 10:1 length to width and a ratio of approximately 365:1 bond pad area to cantilever area. This aspect ratio was chosen to facilitate the successful release of the cantilevers while still maintaining effective adhesion of the bond pad to the substrate. The design is critical to the release method.

The cantilever and bond pad design allow for the bond pads to remain connected to the substrate after release. The bond pad is partially undercut during the release process; however, it remains connected to the silicon surface while the cantilevers are completely freed from the silicon surface.

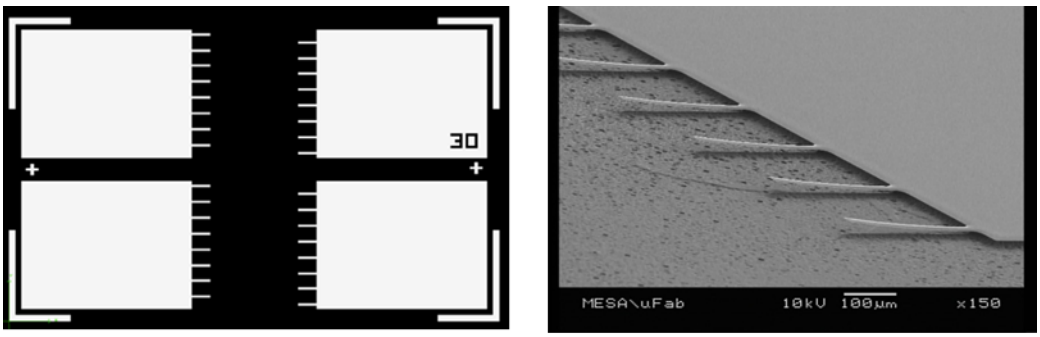

Figure 27: Mask layout (a) and an SEM image (b) of the 30µm wide by 300µm long fabricated beams.

4.2.2 Device Fabrication

To fabricate the carbon MEMS devices, improved reduced graphene oxide (iRGO) is weighed and incorporated into photoresist AZ 4330. The concentrations of iRGO used for this set of experiments were 0.5%, 1.0%, and 2.0 wt.%. The slurry is mixed for 2 hours with sonication to agitate and suspend the iRGO within the photoresist. The AZ 4330 photoresist and iRGO mixture is then manually dispensed onto 100 mm n-type silicon wafer (10-100 ohm-cm) and spin casted at 4000 rpm for 30 seconds, followed by a soft bake at 90^{o}C for 90 seconds on a hot plate. This produces a thin photoresist and iRGO film 3.4 µm thick. The pattern is then exposed onto the coated wafer using a Karl Suss MA-6 manual contact aligner for 30 seconds at a wavelength of 420nm and an intensity of 20mW/cm^2. The exposed wafer is submerged for 90 seconds with heavy agitation into AZ400K 1:4, a buffered KOH based developer leaving the cantilever

pattern. The patterned resist is then cured by baking the wafer at 110°C for 10 minutes, followed by a deep ultra-violet (DUV) exposure in a Fusion F300 UV Curing System at 260 nm with an intensity of 160mW/cm^2, for 30 seconds. A final ramped bake from 100°C to 280°C at a ramp rate of approximately 10 degrees per minute completes the curing process. The resist cures by evolving the majority of the water, CO_2 and CO through decarboxilation and decarbonylation during the baking process. The wafer is then cleaved and baked in a reducing atmosphere of H_2:N_2 (5%:95%) in a Lindberg tube furnace at 1150°C, then soaked for 1 hour and allowed to cool to room temperature via natural convection.

After pyrolyzed carbon conversion, a xenon difluoride (XeF_2) silicon etch release process is performed to remove the silicon from under the graphene stiffened carbon MEMS device. Using an XACTIX e1 Series XeF_2 etch system releases the cantilevers from the substrate after 210 cycles. XeF_2 etchant is a highly selective isotropic etchant for silicon and undercuts the carbon cantilevers releasing them from the substrate, leaving them suspended above the silicon. The XeF_2 vapor is pulsed in cycles in the process chamber, resulting in highly efficient silicon etching. This isotropic etch allows large features to be undercut, etching laterally at nearly the same rate as its vertical etch.

4.2.3 Conductivity Measurements

Four point probe measurements were taken on 2.5 cm x 2.5 cm quartz substrates purchased from GM Associates. The iRGO loading ranged from 0.0 wt.%, 0.5%, 1.0%, to 2.0 wt.% for these samples, along with one standard deviation of 5 recorded measurements. The substrates were processed through the same high temperature reducing atmosphere as the carbon beams to understand the conductivity as a function of iRGO loading. The measurement was performed on a 4-wire NI PXI-4070 Signature conductivity meter with a four point Signatone tungsten carbide probe tips at 1 millimeter spacing. To find the average conductivity (S/cm), five measurements on each sample are collected and supported with thickness verification using cross sectional SEM. The average film thickness ranged between 850 nm and 900 nm and had no bearing on loading. For the conductivity calculation, the 900 nm thickness was chosen and the results, shown in Figure 28, indicate an increase in conductivity with increased iRGO loadings, with an 11% increase in conductivity with 3.1% standard deviation for 2.0 wt% iRGO as compared to 0.0 wt.% pyrolytic carbon.

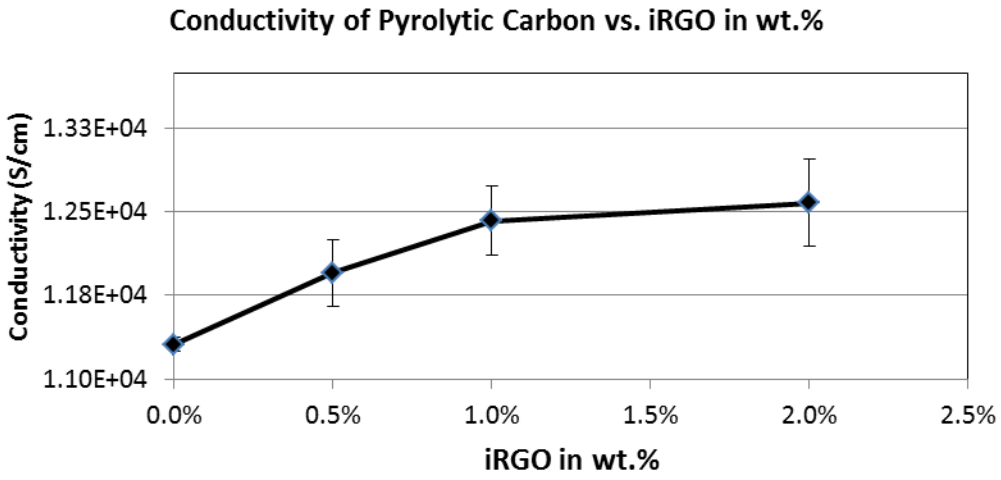

Figure 28: The conductivity of the pyrolyzed carbon vs. iRGO (wt.%) fabricated on quartz substrates.

4.2.4 Laser Doppler Vibrometer (LDV) Measurements

Dynamic measurements were recorded using a scanning laser doppler vibrometer (LDV). A die containing the sample beams was adhered to a piezoelectric shaker on a sizeable mass. A pseudo-random input was used to excite the test pieces with a frequency range of 0 to 1.5 kHz. Single point LDV measurements at the tip of each beam were recorded as well as scans to verify the bending modes. The input voltage to the piezoelectric shaker from the signal generator was used as the reference signal.

A model of a cantilever and gradient-based optimization techniques were used to fit material and geometric parameters to the experimental data. The frequency of the i^{th} bending mode for a homogenous, fixed-free cantilever beam can be written in closed-form, shown by Eq. (12), where L is the length of the beam, E is the Modulus of Elasticity, I is the area moment of inertia about the neutral axis, m is the mass per unit length and λ_i is a constant corresponding to the fixed-free boundary condition [17]. The cross-section of each beam was determined by SEM to be wing-shaped and approximately 1.75 µm at the thickest location. Figure 29 shows an SEM image of a sample cross-section. A semi-elliptical cross-section was assumed for the model, described by Eq. (13) and Eq. (14), where A_c is the cross-sectional area I is the area moment of inertia about the centroid, a is two times the beam width and b is the maximum thickness at the center of the beam [17]. While there is evidence that the beam tip curves up, the assumption is still made that the centroid of the beam lies on the neutral axis.

$$f_i = \frac{\lambda_i^2}{2\pi L^2}\left(\frac{EI}{m}\right)^{\frac{1}{2}} \tag{12}$$

$$A_c = \frac{\pi ab}{2} \tag{13}$$

$$I_{xc} = \frac{ab^3}{72\pi}(9\pi^2 - 64) \tag{14}$$

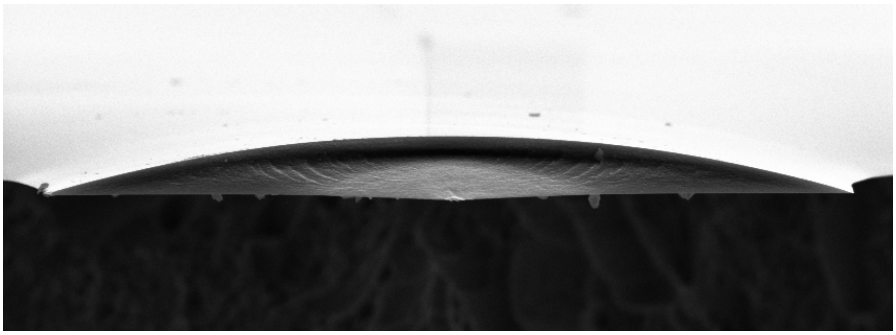

Figure 29: SEM cross-section of a sample cantilever beam with 2.0 wt.% iRGO.

Dynamic tests were performed on a small set of cantilever beams to determine how the amount of iRGO loading changes the frequency response of the system in order to gain insight into the effects of the iRGO on the Modulus of Elasticity. Fixed-free cantilever beams were evaluated in two different sizes, 20 μm X 200 μm and 30 μm X 300 μm long. The test pieces also varied by iRGO loading as samples were fabricated with 0.0%, 0.5%, 1.0% and 2.0 wt.% iRGO loading for both sizes.

Resonant frequency spectra in Figure 31(a) and (b) illustrate the dynamic response of a 30 μm X 300 μm carbon beam as a function of iRGO loading at the first bending mode and second bending mode, respectively. Figure 32 describes the linear relationship of iRGO loading as a function of peak resonant mode from 0.0 wt.% to 2.0 wt.% with R^2 being 0.91 and 0.94 for a fit parameter. The nanomaterial loading in Figure 32 extends to demonstrate and compare engineered beams of a 10:1 aspect ratio have reproducible trends in mechanical rigidity due to the iRGO dispersion and carbonization. Our hypothesis that the mechanism for increased Young's Modulus is that graphene basal plane is providing a scaffold or template to adjust the surrounding amorphous carbon phases is still under investigation as to the actual mechanism.

To support these results, an investigation into beam-to-beam variation of 26 beams with a length of 300 μm and 1.0 wt.% iRGO loading were tested. The average frequency of the first bending mode, Figure 30(a), was found to be approximately 18.47 kHz with a standard deviation of 0.64 kHz.

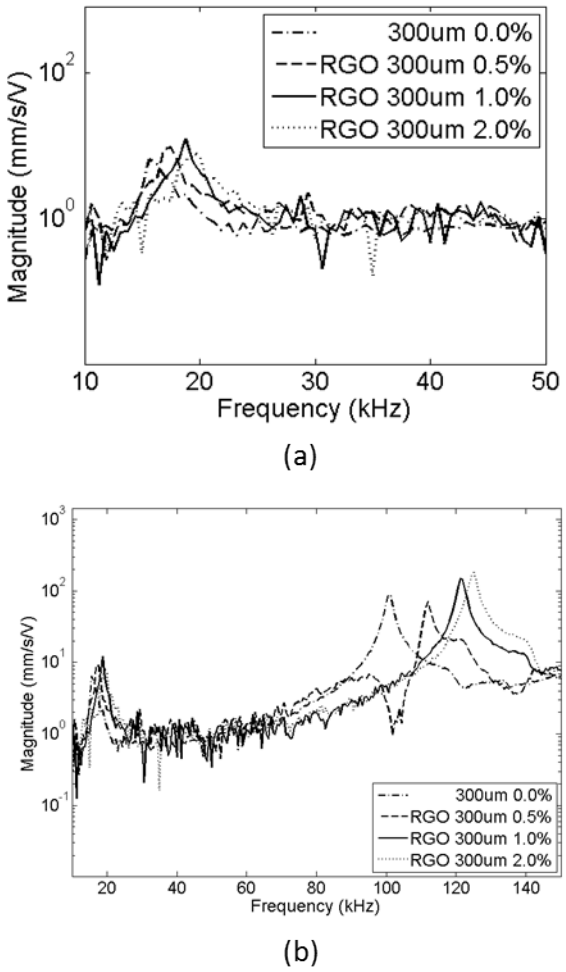

Figure 30: Resonant frequency response for 300 µm long beams for iRGO loadings of 0.0%, 0.5%, 1.0% and 2.0 wt.%, showing the frequency of the (a) 1st bending modes, and (b) the frequency shift of the 1st and 2nd bending modes responses.

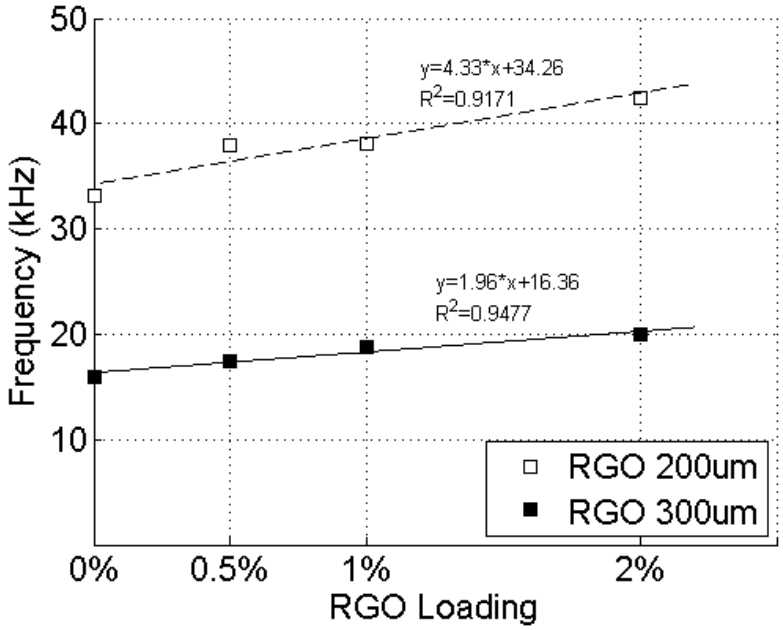

Figure 31: The change in the 1st resonant frequency mode for a 20 µm x 200 µm and 30 µm x 300 µm beam as a function of iRGO loading in wt.%.

The average frequency of the first 3 bending modes was also calculated. For the 200 µm long beam case, the frequencies of the first 3 bending modes increased by approximately 15-20% with the addition of 0.5% RGO loading. That value grows to 25-35% for 2.0% RGO loading. For the 300 µm long beam case, the frequencies of the first 3 bending modes were increased by approximately 8% for 0.5% iRGO loading and 25% for 2.0% iRGO loading.

Figure 32 establishes the relationship to Modulus of Elasticity computed from fitting the measured bending modes to a closed-form beam equation [18]. Parameters chosen for modeling included a density of 1.4 g/cm^3 and maximum thickness at the center of the cross-section, 1.75 µm, with the length of the beam allowed to range from 200-210 µm due to undercut of the etch step in the fabrication process. The largest unknown, the Modulus of Elasticity, was allowed to range between 15 and 100 GPa. The cost function of the gradient-based optimization aimed to minimize the error between the computed natural frequency of the first 3 bending modes from the model and those recorded experimentally in a least-squared fashion. Parameters in the model were fit for 200 µm long beams of each iRGO loading. The optimized Modulus of Elasticity is plotted in Figure 32 and illustrates an increasing trend of moduli for increased iRGO loading. The optimization did not fit the frequencies of the first 3 bending modes perfectly so the percent error was computed. Using these frequency extremes as well as the nominal parameters from the optimization, a range of moduli was computed for each beam type. The maximum and minimum moduli for each beam are shown as the error bars (+/- 10 %) in Figure 32. This analysis indicates the Modulus of Elasticity increases from 41 GPa to 68 GPa, a 65% improvement, by the addition of 2.0 wt.% RGO loading.

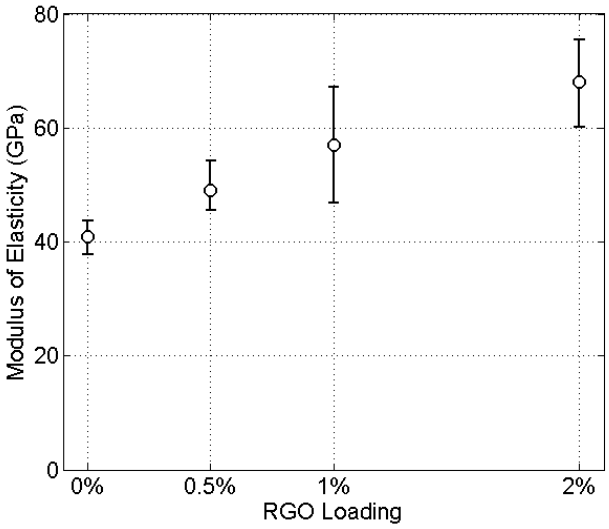

Figure 32: Estimated Modulus of Elasticity for beams loaded with iRGO by fitting the first 3 bending modes computed from a closed-form model of a fixed-free cantilever.

4.3 Summary

The development of a carbon composite incorporating graphene nanomaterial as a stiffener has been demonstrated. The incorporation of graphene leads to an increase in conductivity and Modulus of Elasticity with increasing concentrations. Graphene as a template surface for ordering amorphous carbon during thermal treatment is suggested as a possible reason for these increases, although this still needs verification; however, the electromechanical data indicates this is a viable new approach for developing carbon-carbon composites using photo-sensitive materials as well new tunable device characteristics. In our limited experience, not all nanomaterial fillers behave similarly to graphene under the previously reported conditions [19]. This provides the MEMS community with a new opportunity in materials and device design.

5. IRRADIATION EXPERIMENTS

The effect of total dose gamma irradiation up to 2 Mrad was assessed by measuring the resistance and performing Raman analysis on thin film resistors and clamped-clamped beams (bridges) before and after irradiation from a Co_{60} source. Two experiments were performed during the LDRD. During the first, pyrolyzed carbon resistors and bridge structures were irradiated with doses ranging from 50 krad to 2 Mrad. Due to ambient effects during the first experiment, a second experiment was performed where carbon resistors were irradiated to a dose of 2 Mrad under more controlled ambient conditions.

The resistor die consists of 6 different sized resistors, summarized in Table 5, all having a length/width ratio of 4. The bridge die consists of arrays of 20 parallel bridges that are 400µm long and 10µm wide and separated by 10µm. The fabrication processes of both structures were described previously. The resistors and bridges were fabricated out of pyrolyzed AZ 4330 (unloaded) photoresist. The die were packaged without lids in 24-pin DIP's for testing. For reference, an optical image of a packaged resistor die is shown in Figure 41. The resistance was measured using an LCR meter.

In the first experiment, the devices were subjected to two rounds of irradiation. The resistor dosing is summarized in Table 6. Sample 6R is the control and received no irradiation. Resistance measurements and Raman analysis were performed before and after each dose was administered. The Raman procedure and results are discussed, followed by the resistor measurements.

Table 5: Resistor sizes.

L [µm]	W [µm]	Length/Width
200	50	4
400	100	4
600	150	4
800	200	4
1000	250	4
1200	300	4

Table 6: Gamma ray doses on each resistor die

Resistor Die	Dose1	Dose2
2R	50krad	500krad
4R	100krad	1Mrad
5R	150krad	2Mrad
6R	Control	Control

The raw Raman data are fit using the summation of a Brit-Wigner-Fan lineshape (G-mode) combined with a Lorentzian function (D-mode). An example fit is shown in Figure 33. A 50X/0.55 NA long working distance objective was used. The source power was at or below 10mW, below the 20mW power level that was observed to visibly damage the sample surface. Data was taken from two locations: the center and edge regions of each resistor. At each location a 45µm x 170µm map was acquired with a 1µm separation between acquisition points. The ratio of the intensities of the D-peak at 1350 cm^{-1} and the G-peak at 1600 cm^{-1} (I_D/I_G ratio) provides insight into the disorder of the carbon structure. This and a plot of the G-peak position

are compared to the amorphitization trajectory developed by Ferrari and Robinson [20] to determine the type of disorder and whether the structure is changing as a function of irradiation dose.

Figure 34 shows the Raman spectra from sample R4 measured at doses of 0rad, 100krad, and 1Mrad. The data is representative of all of the samples, both irradiated and the control. The overall shape of the curves is consistent with other reported data [21], and indicates a disordered (non-graphitic) structure. The I_D/I_G ratio and G-peak values are plotted in Figure 35 as a function of dose (upper plots). Following the graphite amorphitization curves discussed by Ferrari and Robinson [20], the films are nanocrystalline with mostly sp_2 bonding. This is consistent with our TEM results.

The overall shape of the Raman spectra is not significantly changed due to irradiation. There could be a slight increase in the I_D/I_G ratio at higher dose levels, although it is mostly unchanged up to 2Mrad. The G-peak position increases slightly at doses ≥500krad. At first glance, it appears that the G-peak position (and possibly the I_D/I_G ratio) may be dose-dependent, however when the G-peak position is plotted as a function of time, as it is in the lower half of Figure 35, this increase can also be explained as a time dependence.

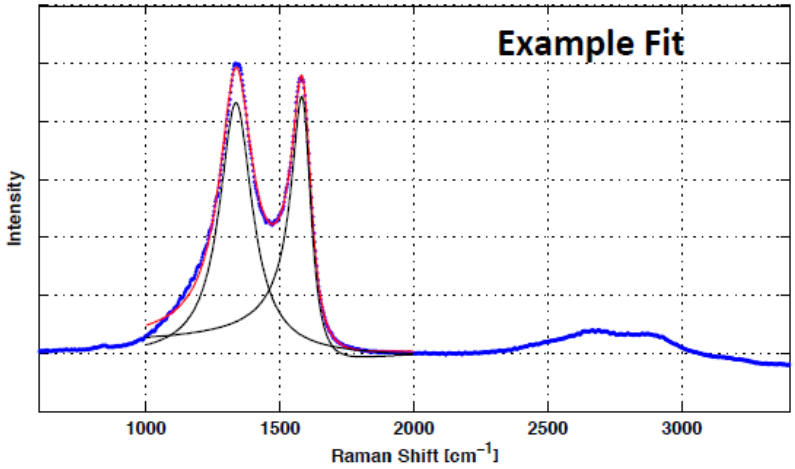

Figure 33: Example fit of the Raman data.

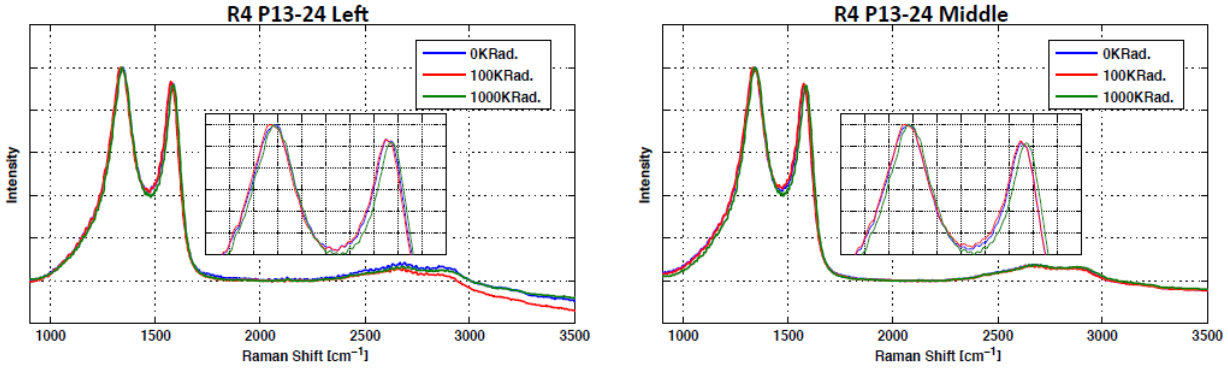

Figure 34: Raman data from sample R4. This is representative of all 4 samples (including the control).

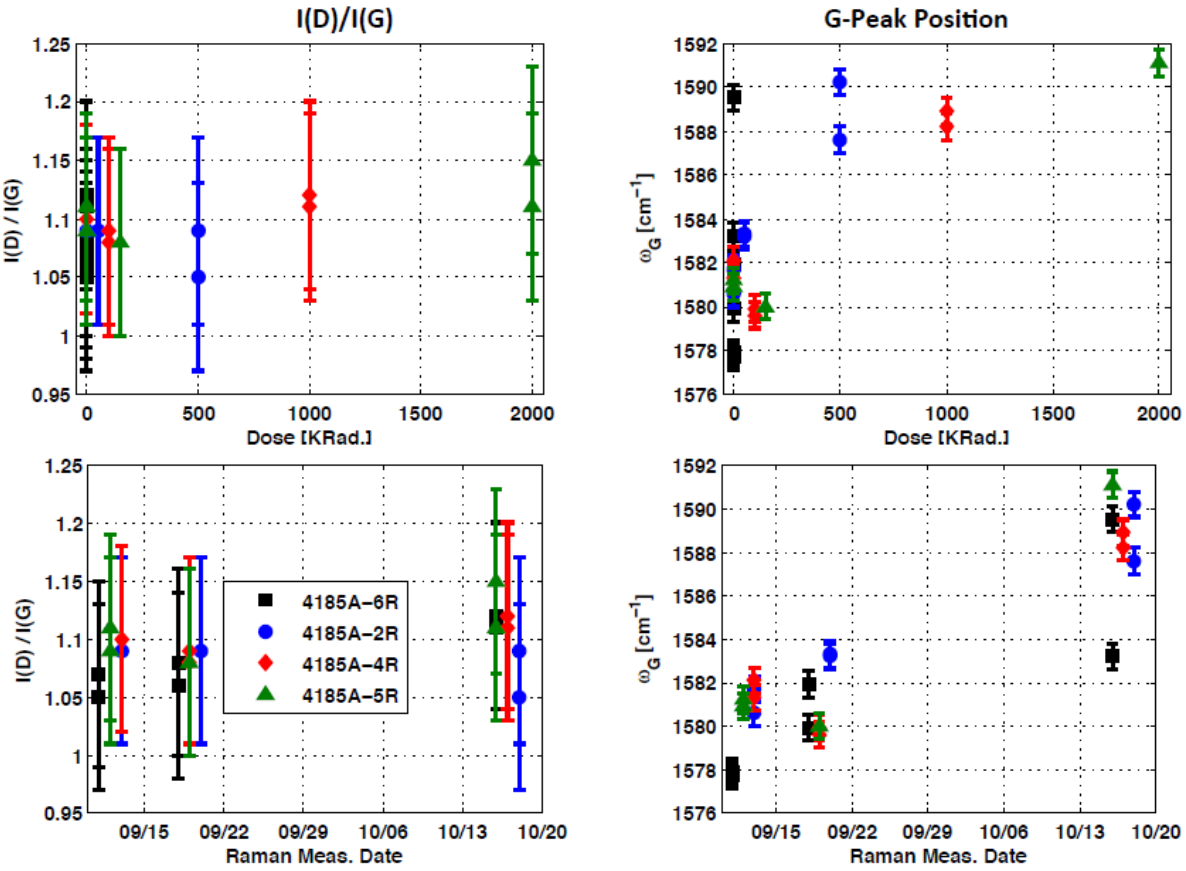

Figure 35: Plots of the I_D/I_G ratio and the G-peak position as a function of gamma dose (top plots) and time (bottom plots).

The resistance measurements of the thin film resistors and the bridges are plotted in Figure 36 and Figure 37 both as a function of dose and time. The resistance of both of the structures appears to have a significant dose dependence. The normalized resistance of the resistors and bridges increases by approximately 5% and 10%, respectively after an exposure of 50krad. However, when the normalized resistance of both structures is plotted as a function of time, including the controls, it is clear that the effects are time dependent.

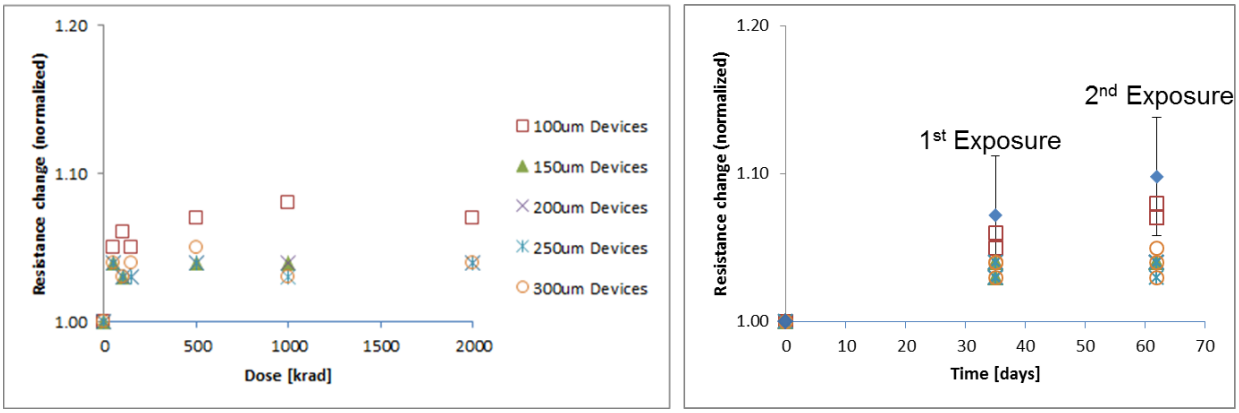

Figure 36: Normalized change in the measured resistance of thin film resistors as a function of gamma irradiation dose (left) and as a function of time (right). The unirradiated controls are also plotted as a function of time (right).

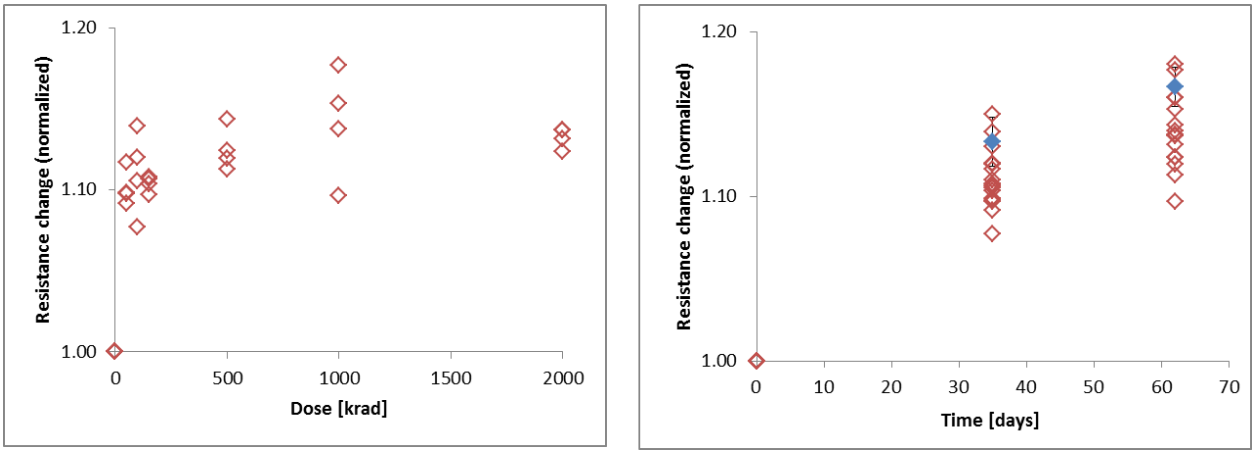

Figure 37: Bridge resistance measurements as a function of dose (left) and time (right). Control (unirradiated) bridges are shown on the right.

Subsequent experimentation using a heated high vacuum chamber revealed that the resistance increases slowly over the course of days to weeks when the devices were left exposed to lab ambient. Putting the devices under vacuum stabilized and eventually decreased the resistance of the structures. Applying heat to the devices under vacuum very rapidly reduced the resistance. Based on this work, we suspect that a slow process of water adsorption was responsible for the resistance increase.

In order to isolate the effects of irradiation from the time-dependent changes in the microstructure and the resistance, a second series of exposures was performed on two packaged resistor die, which were held under vacuum until they were irradiated and exposed. They were analyzed before and after 2Mrad of gamma irradiation from the same Co_{60} source. Chip 5R was irradiated and chip 6R acted as the control and was not irradiated during the experiment. Raman analysis was performed approximately 2 ½ months prior to irradiation. A 50X/0.55 NA long working distance objective was used. The analysis was done at the center of each resistor in a 10µm wide window that spanned its full width. The raw data (colored blue) curves are plotted in Figure 38 and the G-peak and I_D/I_G ratio are plotted in Figure 39. Both packages were then placed into the vacuum chamber for 2 ½ months. During that time, the temperature was cycled

several times from ambient temperature to a maximum of 130°C. The chamber pressure stabilized to 0.06 µTorr. Two days prior to irradiation, the devices were removed from the vacuum chamber and electrically tested. Raman measurements were made one day prior to irradiation (red data markers in Figure 38 and Figure 39), and again the day after they were subjected to 2 MeV (black data markers in Figure 38 and Figure 39).

The overall shape of the curves is similar between the irradiated and control samples. The intensity of the 3 curves was determined to be within measurement error. The background noise of base curves in the raw data plots is higher than the "Pre" and "Post 2MRad" curves. This was attributed to a filter changed made after the "Base" measurements were performed. Similar to the previous data, and despite the fact that the resistors were stored in vacuum between the two measurements made prior to irradiation, there is a slight increase in the G-peak value. Also similar to the previous measurements, the I_D/I_G data is unchanged over the same period. The G-peak and values are unchanged as a result of the gamma exposure.

The resistor values (not shown) decreased while the device was under vacuum and temperature cycled. During that time, the G-peak intensity increased. This increase is similar to the increase observed during the 1st round of exposures when the devices were stored in open ambient. However, during the 1st round of exposures, the resistance increased because it was stored in open ambient. This shows that the G-peak increase is uncorrelated with the resistance change.

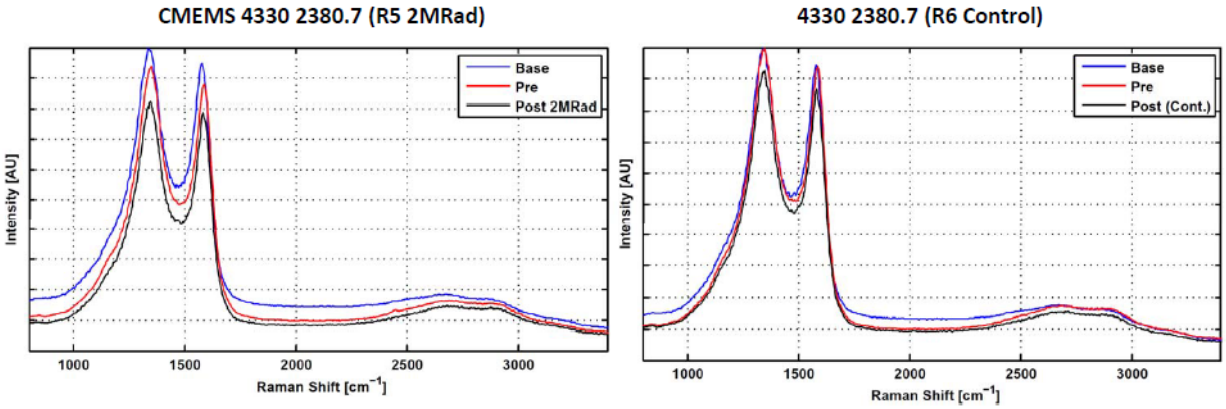

Figure 38: Raw Raman measurement data

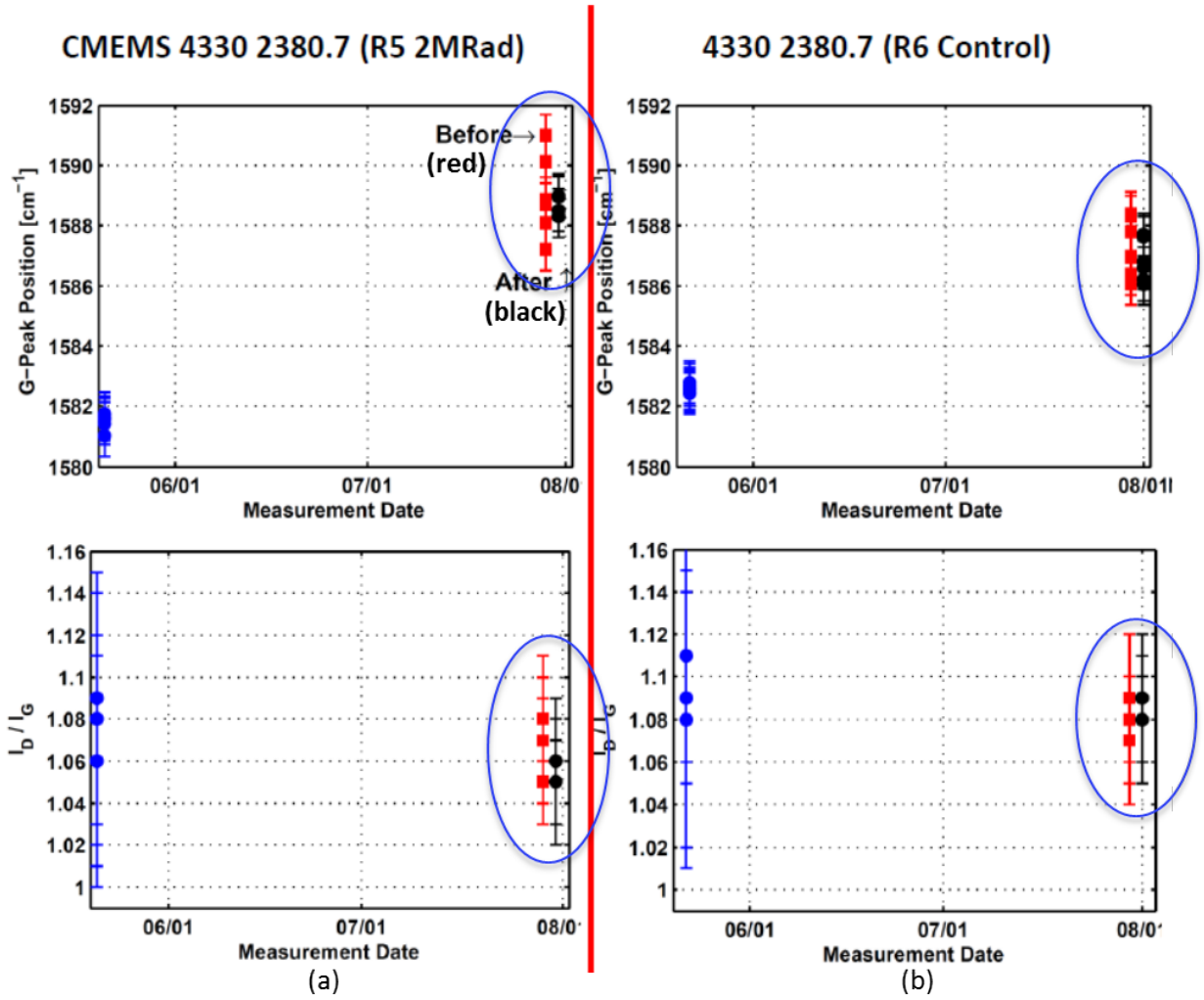

Figure 39: Plots of the G-peak position and I_D/I_G ratio. Neither were changed by the irradiation process (2 Mrad).

6. HERMETIC PACKAGING

Based on our results showing that the resistance of the pyrolyzed carbon increases slowly over a time period of days to months, and that the effect is reversible in by placing the devices in a vacuum environment, it made sense to measure the resistance of hermetically packaged devices in an inert ambient. Resistors were fabricated out of 2 types of photoresists: AZ4330 and 50XT. The AZ4330 devices were additionally split into two different processes. Two of the die were patterned by RIE after the pyrolysis process, and 4 were photo-patterned and developed prior to the pyrolysis process. A total of 8 die were packaged. This is summarized in Table 7.

Table 7: A list of resistor die and photoresist types that were hermitically packaged.

Photoresist	Qty.	Processing	Carbon thickness	Package Names
AZ-4330	2	RIE after pyrolysis	1.5um	R1, R2
AZ-4330	4	Patterned before pyrolysis	1.5um	R1, R2, 2380_R1, 2380_R2
50XT	2	RIE after pyrolysis	2.8um	R1, R2

High-temperature co-fired 24-pin ceramic packages were selected for the experiment. One of the packages is shown in Figure 40. After the die were wire bonded with Au ribbon bonds, the packages were vacuum baked at $4x10^{-4}$ Torr for 2 hours. Immediately after the vacuum bake, the packages were placed in the belt furnace in an N_2 ambient to seal the lids with an 80/20 Au/Sn eutectic. The belt furnace temperature profile is shown in Figure 41.

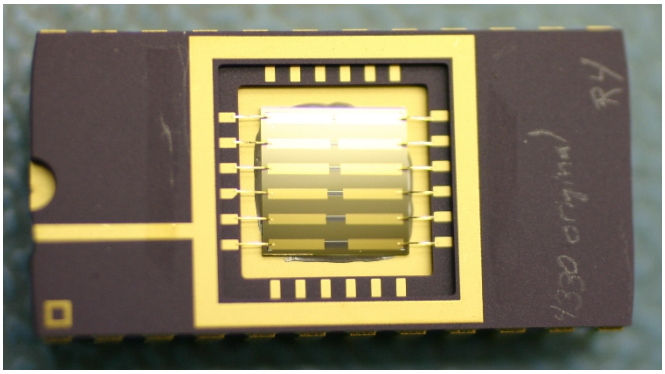

Figure 40: Optical image of a die in a ceramic DIP package prior to the lidding process showing the 5 resistor geometries. All resistors have the same length-to-width of 4. The resistors are Au ribbon bonded at both ends to the ceramic DIP package.

The resistance of each of the resistors was measured prior to packaging, after packaging, then again at intervals of approximately 1 month over the course of 6 months. Representative results are shown in Figure 42. All 6 resistors were measured in each package. The high-temperature packaging process temperature intially dropped the resistance, as shown in the right side of Figure 42. During the 6-month test period, the resistors did not change value. The hermetic seal succeeded in stabilizing the resistor values. This was true for all of the measured resistors, with the exception of the resistors fabricated out of 50 XT. Those resistors slowly failed by open circuit over the course of 6 months. Failure analysis of one of the two packages showed that the structures failed due to poor step coverage of an Au film at the edges of the pyrolyzed carbon resistor. These were the thickest films and the Au was deposited by evaoporatoin, which is a

line-of-sight process. This was not a problem for the other resistor die because those carbon films were not as thick.

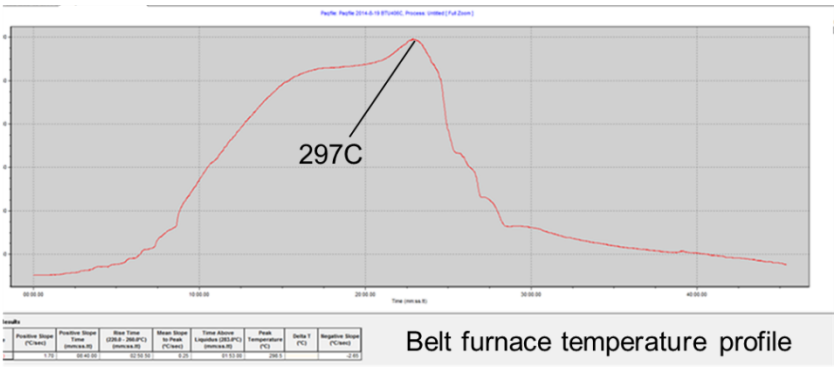

Figure 41: The lids were sealed by 80/20 Au/Sn (280°C eutectic temperature) in a belt furnace using this temperature profile in an N_2 ambient. The belt furnace temperature reached a maximum of 297C during the process.

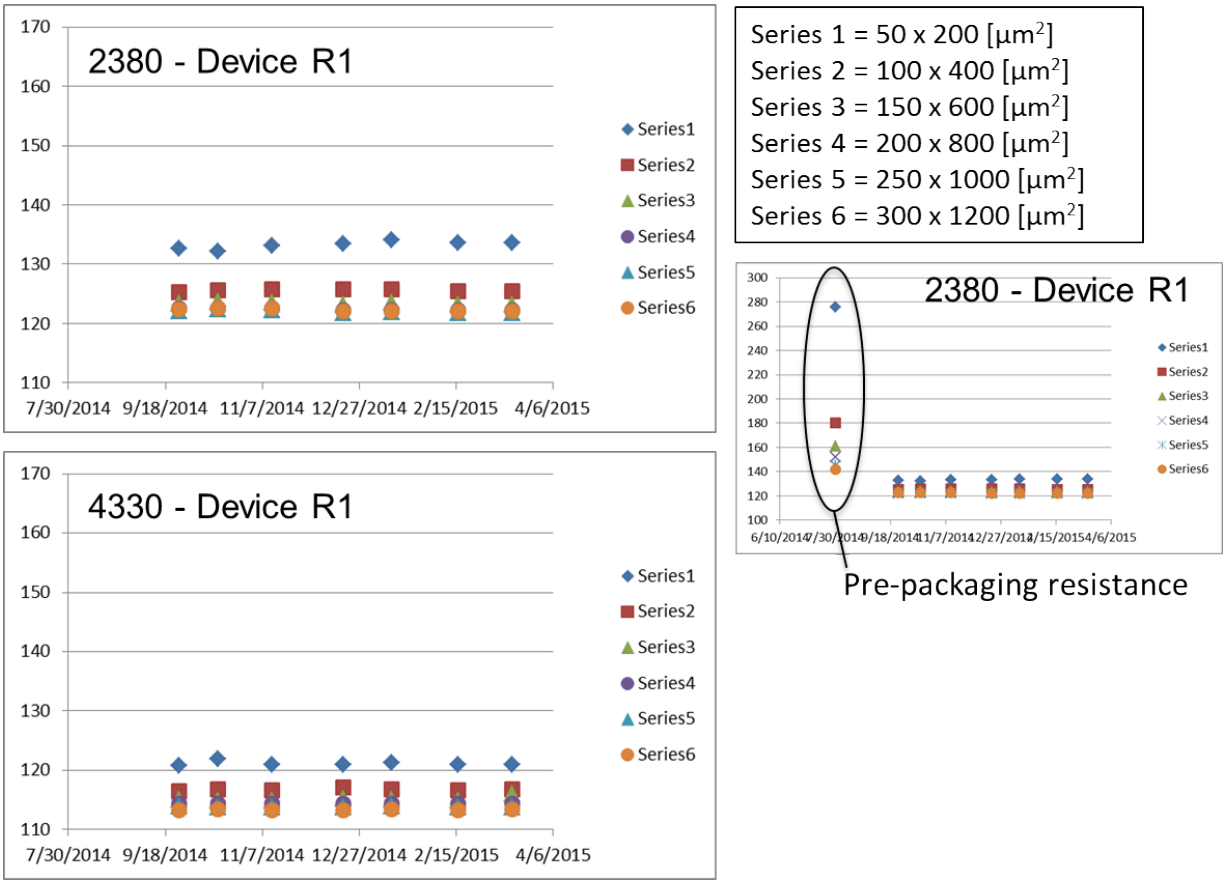

Figure 42: Representative resistance measurements of hermitically packaged PPR resistors. The resistance values are stable over the 6 month data collection time.

7. CONCLUSIONS

Pyrolyzed carbon as a mechanical material is promising for applications in harsh environments. In this LDRD, we characterized the material, and developed novel multi-level and thick film processes for fabricating carbon composite micro-electromechanical systems (CMEMS) structures. A novel method of increasing Young's modulus and the conductivity of pyrolyzed AZ 4330 was demonstrated by loading the films with graphene oxide prior to pyrolysis. TEM results showed the film to be largely amorphous containing some sub-micrometer sized graphite crystallites. This was consistent with our Raman analysis, which also showed the film to be largely sp_2 bonded. The films were found to be tolerant to significant gamma irradiation doses. Resistors survived to high temperatures in an inert ambient. Hermetic packaging stabilized ambient-related changes in film resistance.

8. REFERENCES

1. Whitesides, G.M.; Schueller, O.J.A; Brittain, S.T.; Marzolin, C. *Fabrication and Characterization of Glassy Carbon MEMS*. Chem. Mat. Vol. 9. 1399-1406. 1997.
2. Madou, M.; Wang, C.; Malladi, K.; *Fabrication of suspended carbon microstructures by e-beam writer and pyrolysis*. Carbon. Vol. 13. 2602-2607 2006.
3. McCreery, R.; Ranganathan, S. ; Majji, S.M.; Madou, M. *Photoresist-Derived Carbon for Microelectomechanical Systems and Electrochemical application.* Journal of The Electrochemical Society, Vol. 147. No.1. 277-282. 2000.
4. Burkel, D.B.; Washburn, C.M.; Raub, A.K.; Brueck, S.R.J.; Wheeler, D.R.; Brozik, S.M.; Polsky, R. *Lithographically Defined Porous Carbon Electrodes*, Small. Vol. 5. No. 24. 2792-2796. 2009
5. C. M. Washburn, T. N. Lambert, J. Blecke, D. Davis, P.S. Finnegan, B.G. Hance, D. R. Wheeler, T.E. Beechem, T.M. Alam, M.T. Brumbach, and J.M. Strong, Tunable Young's Modulus in Carbon MEMS using Graphene-based Stiffeners, *ECS Transactions, 2013, vol.50, issue 12, pp. 423-434.*
6. Marcano, D.C.; Kosynkin, D.V.; Berlin, J.M.; Sinitskii, A.; Sun, Z.; Slesarev, A.; Alemany, L.B.; Lu, W.; Tour, J.M. *Improved Synthesis of Graphene Oxide* . ACS Nano. Vol. 4, No. 8. 4806-4814. 2010.
7. M. Strojnik; "Specific Resistivity of Glassy-Carbon and its Temperature Dependence", Unconventional Imaging II, edited by Victor L. Gamiz, Paul S. Idell, Marija S. Strojnik, Proc. of SPIE Vol. 6307, 63070S, (2006).
8. O. J. A. Schueller, S. T. Brittain, C. Marzolin, G. M. Whitesides; "Fabrication and Characterization of Glassy Carbon MEMS", *Chem. Mater*. 1997, 9, 1399-1406.
9. A. Singh, J. Jayaram, M. Madou, S. Akbar; "Pyrolysis of Negative Photoresists to Fabricate Carbon Structures for Microelectromechanical Systems and Electrochemical Applications," *Journal of The Electrochemical Society*, 149 (3) E78-E83 (2002)
10. M. Liger, T. Yu-Chong; "A 32*32 Parylene-Pyrolyzed Carbon Bolometer Imager", *MEMS 2006*, Istanbul, Turkey, 22-26 Jan. 2006, pg. 106.
11. R. A. Wood, "Monolithic Silicon Microbolometer Array", *Semiconductors and Semimetals*, Vol 47, 1997.
12. D. Halliday, R. Resnick; "Physics: Parts I and II," John Wiley and Sons, New York, New York, (1978) pg. 481.
13. S. Berber, K. Young-Kyun, D. Tománek; "Unusually High Thermal Conductivity of Carbon Nanotubes", Physical Review Letters, Vol. 84, No. 20, 15 May 2000, pg. 4613.
14. A. A. Balandin, S. Ghosh, W. Bao, I. Calizo, D. Teweldebrhan, F. Miao, C. Ning Lau; "Superior Thermal Conductivity of Single-Layer Graphene," Nano Lett.,Vol. 8, No. 3, 2008, pg. 902.
15. Bunch, J.S.; Van der Zande, A.M; Verbridge, S.S.; Frank, I.W.; Tanenbaum, D.M.; Parpia, J.M.; Craighead, H.G.; McEuen, P.L. *Electromechanical Resonantors from Graphene Sheets*. Science. vol. 315. 490-493. 2007
16. Zalalutdinov, M.K; Robinson, J.T., Junkermeier, C.E.; Culbertson, J.C.; Reinecke, T.L.; Stine, R.; Sheehan, P.; Houston, B.H.; Snow, E.S. *Engineering graphene mechanical systems*. ACS Nano Letters. DOI: 10.1021/ nl3018059, 2012

17. Lambert, T.N.; Luhrs, C. C.; Chavez, C. A.; Wakeland, S.; Brumbach, M.T.; Alam, T.M. *Graphite oxide as a precursor for the synthesis of disordered graphenes using the aerosol through plasma method*. Carbon. Vol. 48. 4081-4089. 2010
18. Stankovich S, Dikin DA, Piner RD, Kohlhaas KA, Kleinhammes A, Jia Y, et al., *Synthesis of Graphene-Based Nanosheets Via Chemical Reduction of Exfoliated Graphite Oxide*. Carbon. Vol. 45. 1558-1565. 2007
19. Blevins, Robert D., 1979, *Formulas for natural frequency and mode shape* Van Nostrand Reinhold Co., New York.
20. A. C. Ferrari and J. Robertson, *Interpretation of Raman spectra of disordered and amorphous carbon*, Physical Review B, Vol. 61, No. 10, 2000.
21. S. Ranganathan, R. McCreery, S. M. Majji, and M. Madou, Photoresist-Derived Carbon for Microelectromechanical Systems and Electrochemical Applications, J. Elec. Soc., 147 (1), pp. 277-282, (2000).

DISTRIBUTION

1	MS0346	Jill Blecke	1526
1	MS0346	Michael Satches	1526
1	MS0886	Patrick Finnegan	1853
1	MS1212	Chris Dyck	5965
1	MS1212	Cody Washburn	5965
1	MS1212	Michael Rector	5965
1	MS1415	Thomas Beechem	1124
1	MS1425	Kent Pfeifer	1714
1	MS0899	Technical Library	9536 (electronic copy)
1	MS0359	D. Chavez, LDRD Office	1911


Sandia National Laboratories